

**ON THE SETTLING OF SPHERICAL PARTICLES IN POWER-LAW FLUID
AT MODERATE REYNOLDS NUMBER**

Marco A. Ferrari*, Alan Lugarini, Admilson T. Franco

Research Center for Rheology and Non-Newtonian Fluids (CERNN), Postgraduate Program in Mechanical and Materials Engineering, Federal University of Technology – Paraná (UTFPR), Curitiba, PR, 81280-340, Brazil.

marcoferrari@alunos.utfpr.edu.br

alansouza@utfpr.edu.br

10 admilson@utfpr.edu.br

20

©2022. This manuscript version is made available under the CC-BY-NC-ND 4.0 license

<https://creativecommons.org/licenses/by-nc-nd/4.0/>

* Corresponding Author

ABSTRACT

The present paper analyses the settling behavior of multiple spherical particles in a power-law fluid. The results were numerically solved by the lattice Boltzmann method for the fluid mass and momentum equations and the immersed boundary method for the particle dynamics. The transient particle position and velocity data were obtained for a constant Archimedes number of 1000 and density ratio of 2.25. The objects of the investigation were the solid volume fraction, between 0.2% and 3.3%, and the power-law index, from 0.6 to 1.25. The particles repel each other and avoid collision due to increased fluid viscosity in their gaps for the shear-thickening fluid. On the other hand, for shear-thinning fluids, a wake of low viscosity is formed behind the particles, which leads to a high occurrence of particle collisions. However, as the solid volume fraction increases, these effects become less noticeable, mainly because the settling transitions from viscous to collision-dominated. In all cases analyzed, the average terminal velocity was below the terminal velocity of a free particle.

40

Keywords: Particle settling, hindered settling, power-law fluid, lattice Boltzmann method, immersed boundary method.

1. INTRODUCTION

The movement of multiple non-Brownian particles in a fluid is encountered in many industrial segments, from food processing to oil and gas exploration [1]. The solution of the flow over a single sphere dates back to Stokes [2], and it was later extended to moving particles at higher Reynolds numbers and different densities ratios [3–6], as well as to non-Newtonian fluids [7–10]. When two vertically aligned particles are settling, they often follow the draft-kissing-tumbling process (DKT) described by Fortes et al. [11]. In this process, the trailing particle will approach the leading particle due to the reduced drag in its wake, guiding to the particle touch and a consequent tumbling of one particle over the other, followed by a side-by-side settling motion of the two. For non-Newtonian fluids, the orientation of the particles at a steady-state will depend on the fluid's rheology [12–14]. In shear-thinning fluids, the wake of a leading particle has a reduced viscosity since the wake is generally a high shear region. So, the wake of reduced viscosity attracts and helps to accelerate a trailing particle, keeping it inside the wake until the collision occurs [12,13,15,16]. The knowledge about settling a single or two particles is a good first indicator for multiple particle settling. However, the objects' interactions make the multiple particles settling a highly challenging problem to solve in some cases.

The multiple particles settling problem has a kinematic correspondence to the fluidization process [17,18], in which the particles are subject to counter-flow and have zero displacements on average. When particles settle, they displace fluid in the opposite direction. The force necessary to do so depends on the fluid viscosity and the distance from other particles and walls. As the concentration of particles in the system increases, the drag force exerted on the particles also increases, reducing the settling velocity.

Occasionally, the counter-flow is strong enough to move some particles upwards for a brief period [19].

70 The complexity of this problem has stimulated the development of homogeneous approaches. In such approaches, the relationship between settling velocity and particle concentration is often represented by hindered settling correlations. For instance, the popular correlation from Richardson and Zaki [20] is $U = U_t (1-\phi)^j$, where ϕ is solid volume fraction, U_t is the terminal velocity of a single particle, and j is a fit parameter that depends on the Reynolds number [21]. However, some earlier [22,23] and recent [24–27] studies have shown Richardson and Zaki’s correlation discrepancies. For low solid volume concentration ($\phi \approx 1\%$), and depending on the Archimedes (or Galileo) number, the settling velocity of multiple particles could be higher than a single isolated particle. The effect is associated with the particles grouping together and settling as a
80 larger object. The counter-flow generated is then located in the surroundings of the particle cluster and, therefore, will have a reduced effect on the mean particle settling velocity [25,26].

For non-Newtonian fluids, Chhabra et al. [28] examined the experimental data present in the literature and proposed a correlation for the terminal Reynolds number as a function of the Archimedes number and the power-law index, which allows the estimation of the drag coefficient. Chhabra et al. [28] work was further extended by Chhabra et al. [29], with an experimental evaluation of particles with diameter 0.6 mm to 3.3 mm, density ratio (ρ_s/ρ_f) 2.6, and solid volume fraction of 15% to 43%. The average terminal velocity behaved similarly to a Newtonian fluid for shear-thinning fluids in the
90 range $n \approx 0.8$ to 1.0.

Allen and Uhlherr [30] analyzed the settling of glass particles with a diameter between 0.5 and 1 mm and a density ratio of 2.8 for different shear-thinning viscoelastic

fluids. The solid volume fraction ranged from 5% to 45% in their experiments. They observed that the formation of “fingers” in shear-thinning fluids with $n \approx 0.6$ looked similar as in the settling in Newtonian fluids with bi-disperse solutions [31] or high Archimedes number [25,26]. The “fingering” takes place in the phase separation processes, in which one phase permeates the other in filament structures. In the case of multiple particle settling, the “fingering” occurs when some particles group together and move in columnar structures. For moderately shear-thinning fluids ($n \approx 0.8$), the experiments by Allen and Uhlherr [30] revealed that the columnar structures were substituted by “fluid bubbles” that move in the upward direction.

Daugan et al. [32] studied the settling of spherical particles with a diameter of approximately $95 \mu\text{m}$ and density of 3760 kg/m^3 in Xanthan gum solution. The solid volume fraction varied from 0.3% to 7%. They reported the same formation of columnar structures, and the number of occurrences increased with the solid volume fraction. Moreira et al. [33] studied the multiple particles settling in Xanthan gum solution with a slightly higher particle diameter ($\approx 190 \mu\text{m}$) and lower density ratio (2.75). The columnar structures were also observed in their experiments. They showed that a batch settling in the shear-thinning fluid has a higher settling velocity than a Newtonian fluid. However, the clear-water interface moved slower with the shear-thinning fluid due to the high viscosity in slow-moving fluid.

Alghalibi et al. [34] numerically investigated the settling behavior of spherical particles with a density ratio of 1.5 in Newtonian fluid and shear-thinning fluids between two parallel plates. The solid volume fractions analyzed range was between 1% and 20%. They concluded that two effects compete to dictate the settling regime: the hindered settling, which decreases the velocity with the increase of solid volume fraction, and the shear-thinning effect, which increases the settling velocity with the increase of the solid

volume fraction. In a shear-thinning fluid, the particles tend to come closer together in a side-by-side configuration compared to a Newtonian fluid.

120 The knowledge of multiple particle settling in Newtonian fluids is extensive in the specialized literature. However, for non-Newtonian fluids, the body of work is scarce and unconsolidated, particularly concerning the hindered settling. A computational solution is an exciting approach to provide physical insight into the non-Newtonian phenomenon because it isolates the effects of individual rheological properties. Furthermore, a heterogeneous approach for the solid and fluid phases allows tracking each particle and extracting insightful statistical information from their history. In this work, we utilized the lattice-Boltzmann method (LBM) coupled with the immersed boundary method (IBM) to solve the multiple particle settling problems in a tri-dimensional boundless domain. We focus on a solid volume fraction range of 0.2% to 3.3%, a density ratio of
130 2.25, and a power-law index of 0.6 to 1.25. The consistency index is varied to keep the power-law Archimedes number constant at 1000 [28]. These parameters are similar in order of magnitude to the problem of the cuttings transport in oil and gas wellbores [35] when there is a fluid circulation stoppage.

In this work, the sections are organized as follows. Section 2 presents the governing equations for the particle settling problem in a power-law fluid. Section 3 summarizes the numerical methodology used to solve fluid flow, particle motion, and collision forces. It also shows selected validation cases for particle-particle interaction and non-Newtonian fluid-particle coupling. Section 4 presents the results and discussions for multiple particle settling cases in a shear-thinning fluid.

140

2. BALANCE EQUATIONS

We consider a collection of spheres of diameter D and density ρ_s , placed in the domain randomly at time $t = 0$. The particles are immersed in a power-law fluid and settle under gravity's action. There is no external driving force for the fluid. The fluid motion is governed by the mass and momentum balance equations:

$$\nabla \cdot \mathbf{u} = 0 \quad (1)$$

$$\rho_f \left[\frac{\partial \mathbf{u}}{\partial t} + (\mathbf{u} \cdot \nabla) \mathbf{u} \right] = \nabla \cdot \boldsymbol{\tau} - \nabla P + \rho_f \mathbf{g} + \mathbf{F} \quad (2)$$

where ρ_f is the fluid density, \mathbf{u} is the fluid velocity, $\boldsymbol{\tau}$ is the extra stress tensor, P is pressure, \mathbf{g} is the gravity acceleration, and \mathbf{F} is a body force used to input the momentum transfer from the solids. The extra stress tensor depends on the constitutive equation for the fluid. For a generalized Newtonian fluid of the power-law type, the extra stress tensor relates to the rate-of-strain tensor as [36]

$$\boldsymbol{\tau} = m \|\dot{\boldsymbol{\gamma}}\|^{n-1} \dot{\boldsymbol{\gamma}} \quad (3)$$

where m is the consistency index, n is the power-law index, and $\dot{\boldsymbol{\gamma}} = \nabla \cdot \mathbf{u} + (\nabla \cdot \mathbf{u})^T$ is the rate-of-strain tensor. The power-law index $n = 1$ returns a Newtonian fluid, while $n < 1$ is a shear-thinning fluid and $n > 1$ is a shear-thickening fluid (viscosity increases with $\|\dot{\boldsymbol{\gamma}}\|$). Newton's second law obtains the particle motion for translation and rotation:

$$V_s \rho_s \frac{d\mathbf{U}}{dt} = \int_{\Gamma} \boldsymbol{\sigma} \cdot d\mathbf{S} + (\rho_s - \rho_f) V_s \mathbf{g} + \mathbf{F}_c \quad (4)$$

$$\mathbf{I} \frac{d\boldsymbol{\omega}}{dt} = \int_{\Gamma} (\mathbf{X} - \mathbf{X}_p) \times \boldsymbol{\sigma} \cdot d\mathbf{S} + \mathbf{T}_c \quad (5)$$

where V_s is the particle volume, ρ_s is the particle density, and \mathbf{U} is the translational particle velocity. The integral term in RHS of Eq. (4) represents all forces acting on the particle's

surface (subtracted the hydrostatic pressure). In Eq. (5), \mathbf{I} is the particle moment of inertia, and $\boldsymbol{\omega}$ is the angular velocity, while the integral term in the RHS represents the moments caused by all forces on the particle's surface. The force and torques that originate from particle collisions are \mathbf{F}_c and \mathbf{T}_c , respectively.

We normalize the governing equations with the particle diameter (D) as a length scale, and the settling velocity of a free spherical particle in a given power-law fluid (U_s) as a velocity scale:

$$170 \quad U^* = \frac{U}{U_s}; \quad t^* = \frac{t}{D/U_s}; \quad x^* = \frac{x}{D} \quad (6)$$

The following non-dimensional numbers arise from the normalization. The Reynolds number [28]

$$\text{Re}_D = \rho_f U^{2-n} D^n / m, \quad (7)$$

the density ratio

$$\rho_r = \frac{\rho_s}{\rho_f}, \quad (8)$$

together with the solid volume fraction

$$\phi = \frac{V_s}{V}, \quad (9)$$

and the power-law index n , form the analyzed parameter set of the problem. The particle's contact forces are modeled with constant parameters (see Sec. 4 for values). Chhabra [28]

180 additionally defines the Archimedes number for a power-law fluid as

$$\text{Ar} = \frac{4}{3} g D^{\frac{2+n}{2}} (\rho_s - \rho_f) \rho_f^{\frac{n}{2}} m^{\frac{2}{n-2}}. \quad (10)$$

which is more convenient to use as a parameter instead of Re_D as it represents the ratio between the difference of gravitational and buoyant forces with viscous forces, and because the Reynolds number can only be known *a posteriori*.

3. NUMERICAL METHODOLOGY AND VALIDATIONS

The numerical method employed in this work is similar to the one used in previous work [10], and for completeness, it will be reproduced in Appendix A. The lattice Boltzmann method (LBM) is used for the fluid mass and momentum balance equations, and the immersed boundary method (IBM) solves particle dynamics. Particle collisions
190 are handled by the Hertzian contact model with the normal collision force given by a spring dash-pot system [37].

Four tests were performed to validate the numerical method: i) Poiseuille flow of power-law fluid, ii) particle settling in a power-law, iii) inelastic particle rebound in a Newtonian fluid, and iv) particle collision against an inclined plane.

3.1 Poiseuille flow of power-law fluid

The first validation case is the Poiseuille flow of power-law fluid between two parallel plates. The no-slip condition is imposed by the bounce-back boundary condition [38]. The number of LBM lattices in the normal direction is N . The boundary conditions are periodic in the other directions. A constant body force drives the flow in the z -
200 direction, and the simulation is performed until a steady-state is achieved. Three power-law indexes are evaluated: 0.5, 1.0, and 1.25. The relaxation frequency is the same for all cases $\omega = 1/0.9$, while the maximum velocity is below 0.01 (to reduce compressibility errors). We compare the numerical results with the analytical solution. The error is assessed through the quadratic error norm, defined as

$$\varepsilon_{L_2} = \sqrt{\frac{\sum (\theta_n - \theta_a)^2}{\sum \theta_a^2}} \quad (11)$$

where θ_n is the numerical result and θ_a is the analytical solution of the velocity field. The results are presented in Fig. 1. The error magnitude increases when n diverges from Newtonian, similar to [39] because the numerical viscosity assumes very high values. It can be noticed that the error decay order for $n = 1.0$ and 1.25 is approximately 2, while for $n = 0.5$, it is somewhere between 1 and 2 (1.65 to be precise). The overall error decay order obtained by the present method is situated between the implementations of Gabbanelli et al. [39], and the slightly more complex method of Wang and Ho [40]. We consider that the error decay obtained for power-law fluids is satisfactory for the present work.

3.2 Particle settling in a power-law fluid

To further evaluate the fitness of the numerical method with a power-law fluid, we investigated the drag coefficient of a spherical particle settling in a quiescent fluid. The results obtained by this test will also be necessary for the case of multiple particle settling, as it will provide the settling velocity necessary to normalize the results. A single particle with a diameter of 20 LBM lattices and density ratio $\rho_r = 2.25$ is released from rest in a domain with dimensions $8D \times 8D \times 128D$, with a periodic boundary condition in the transversal direction to mitigate wall effects on the drag coefficient [41]. The terminal velocity and drag force are computed to obtain the drag coefficient value. The power-law index is varied from 0.60 to 1.25. The results are exposed in Table 1. The simulation results agree well with correlations proposed by other works [42–44], under their validity range for n . The comparison for a shear-thickening fluid with references [42,43] diverged due to the correlation not supporting $n > 1$. However, for $n < 1$, an acceptable relative deviation was obtained ($< 10\%$). The relative error for $n = 0.6$ with [43] can be explained because it is within the limit of Re validity. The comparison with reference [44] exhibits

230 good agreement with all n and Re tested. Hence, we assume that the numerical method implemented in this work appropriately represents the fluid dynamics of power-law fluids.

3.3 Inelastic particle rebound in a Newtonian fluid

We consider the case of a spherical particle settling in a tank filled with Newtonian fluid. The particle collides and rebounds on the bottom with a certain loss of kinetic energy. For validation purposes, we compare the simulation results with the experimental data of Gondret et al. [45]. The fluid is silicon oil with a density of 935 kg/m^3 and viscosity of $10 \times 10^{-3} \text{ Pa.s}$. The particle is steel with diameter of 3 mm, density of 7800 kg/m^3 , $E = 240 \text{ GPa}$, and $\nu = 0.3$. The tank bottom is made of soda-glass ($E = 60 \text{ GPa}$ and $\nu = 0.24$).

240 The normal restitution coefficient between the steel particle and soda-glass surface is 0.97 [45]. The numerical domain is discretized with $160 \times 160 \times 800$ LBM nodes. The spherical particle has a diameter of 20 LBM nodes and has its center initially positioned 112mm from the domain floor to guarantee it reaches a terminal velocity before the impact. The bottom and top of the domain are modeled as walls, while the laterals are periodic to reduce wall effects. The relaxation time is $\omega = 1.99282$, and the corresponding time step is $1.24 \times 10^{-6} \text{ s}$. The particle velocity and trajectory results are shown in Fig. 2 and Fig. 3, respectively.

The simulations presented a reduced terminal velocity compared with the experimental data (around 5% relative error). The lubrication force [46] acts to reduce
250 the particle velocity. However, no significant improvement was distinguished with its inclusion. The particle proceeds with multiple collisions until it stops. The numerical method implemented captured the number of collisions and the peak velocity after each rebound, using a spring dash-pot soft-sphere model for the collisions.

3.4 Particle collision against an inclined plane

On this validation test, we analyze the case of a translational sphere colliding with an inclined plane. After the collision, the particle acquires a rotational velocity, which depends on the plane's inclination. The numerical results contrasted with Kharanz et al. [47] experimental data. In their experiment, the spherical particle, made of aluminum oxide ($E = 360$ GPa, $\nu = 0.23$), with diameter of 5 mm (discretized in 20 LBM nodes) collides with a soda-lime glass ($E = 70$ GPa, $\nu = 0.25$) at a velocity of 3.9 m/s. According to Kharanz et al. [47], the normal restitution coefficient is 0.98, and the friction coefficient is 0.0923. We simulate with a time-step of 6.41×10^{-7} s.

The results for the obtained rotational velocity as a function of the impact angle are shown in Fig. 4. Two types of motion can occur during the collision: rolling and sliding. For small collision angles ($0^\circ < \theta \lesssim 30^\circ$), the particle performs a rigid body rolling, while for $30^\circ \lesssim \theta$, it slides and rolls. The simulation results agree well with the experimental data for the sliding regime. However, the rotational velocity obtained is slightly lower for the rolling regime. The difference can be explained by analyzing the rebound angle of the contact patch, shown in Fig. 5. Although a good agreement is found for the rebound angle of the center of mass, there is a visible deviation in the rolling region for the contact patch, which occurs because the model represents only a rolling condition, and therefore micro slips that may occur [48,49] during the rolling are not modeled. The lack of this modeling makes the tangential restitution coefficient also diverge (see Fig. 6). With the present method, the sliding regime is well represented, and for the rolling regime, the tangential restitution coefficient keeps a constant value of $5/7$ [50]. Considering the goals of this work and the characteristics of particle-particle collisions, we consider the implemented numerical method satisfactory.

4. RESULTS AND DISCUSSION

This study is conducted with spherical particles with diameter $D = 20$ (lattice units) and density ratio equal to $\rho_r = 2.25$. The particles are initially randomly placed in a periodic domain of dimensions $12D \times 12D \times 60D$, with zero translational and rotational velocities. The computational domain is periodic in the two horizontal directions. The continuous settling is accomplished by removing the particles that reach the bottom of the domain and reinjecting them at the top with the same velocity when removed. The top and bottom boundaries have zero liquid mass flux, which prevents the fluid from accelerating. The simulations ran for an equivalent time of $tU_s/D = 600$. We consider the solid volume fractions: $\phi = 0.2\%$, 1% , and 3.25% , which corresponds to 33, 165, and 536 particles, respectively. The fluid power-law index is analyzed for $n = 1.25$, 1.00 , 0.75 , and 0.60 . The consistency factor (m) is varied depending on n , keeping the Archimedes number defined by the Eq.(10) constant at 1000. The mechanical properties of the particles are $E = 2$ GPa, $\nu = 0.3$, $e = 0.9$, and $\mu = 0.2$. The free particle velocity used for these cases can be obtained based on C_D results from Table 1. A snapshot of the liquid and solid velocities in the computational domain is exhibited in Fig. 7.

4.1 Particle velocity distributions

The first analysis encompasses the velocity distribution functions and how it depends on the solid volume fraction and power-law index. The results are compiled in Fig. 8. For the settling velocity (vertical component), the mean velocity reduces with n independently of the concentration analyzed (see Table 2). The solid volume fraction makes the hindered settling more significant, as reported in the literature for Newtonian fluids [20]. During the post-processing of simulations, it was observed that, despite the

hindered settling, there were occasions of individual particles settling with a velocity greater than U_s . In the cases analyzed, any occurrence of upwards motion was observed, as occasionally reported in the literature for moderate ϕ [19]. An intriguing aspect of the velocity distribution function is that for $n = 1.25, 1.0$, and 0.75 , independently of the solid volume fraction, the particles presented a positive skewness, while for $n = 0.60$, the skewness was negative; indicating the possibility of two different settling regimes being obtained when changing the power-law index. A summary of the statistical data is given in Table 2. The two different regimes could be correlated with the single-particle Reynolds number, values displayed in Table 1. For low Reynolds numbers, the particles
310 spend more time inside others' wake, increasing their velocity until the collision, causing a positive skewness in the settling velocity distribution. For a relatively high Reynolds number (low n), the settling motion is dominated by inertia, making it difficult for trailing particles to stay in the wake. The negative skewness is then preponderant. The tumbling phase of the DKT is likely to be associated with the presence of lower terminal velocity in the distribution. During this process, the settling velocity of the particles reduces [51]. After that, the particles are surrounded by a relatively low viscosity fluid, and they will take time to reach their terminal velocity [9], negatively skewing the distribution. With the increase in the solid volume fraction, the viscosity field becomes more homogeneous, and these effects are less severe, which can be noted by a reduced skewness magnitude.

320 The hypothesis of two different regimes is further enhanced by analyzing the behavior of the lateral (perpendicular to gravitational field) velocity distribution functions in Fig. 8.d-f. For $n = 0.6$, the particles exhibit a higher frequency of lateral motion and lower kurtosis (see Table 2) since the shear-thinning effect reduces the probability of high lateral velocities. The particles did not show a preferential horizontal movement direction.

Also, the mean lateral velocity was nearly 0 in all cases, and no preferential skewness was noticed.

We also evaluated the angular velocity distributions. The probability distribution functions for settling and lateral directions are shown in Fig. 9. Focusing first on angular velocity in the lateral direction, the decrease in the power-law index causes a decrease in the rotation magnitude. However, as soon as n is equal to 0.6, there is an increase in the particle angular velocity, indicating two different regimes again. The increase in the mean angular velocity from $n = 0.75$ to 0.60 reduces as the solid volume fraction increases, which could be associated with an increase of particle collisions that do not allow them to rotate in the same direction for long periods. The probability distribution function acquires the observed shape because it combines two probability distribution functions (ω_x and ω_y), making the probability of null angular velocity in both lateral directions inferior to the probability of a finite angular velocity magnitude. As a note, the magnitude of the Pearson correlation coefficient of ω_x with ω_y oscillates between 0.25 for $\phi = 0.2\%$ and 0.01 for $\phi = 3.3\%$.

Regarding the angular velocity in the settling direction, either the power-law index or the solid volume fraction increases the variance of the angular velocity, which could be explained by the fluid viscosity being reduced near the particle in both scenarios, allowing it to spin with less resistance. Similar to Fornari et al. [19], the more particles are in the domain, the more flat the distribution is.

4.2 Particle's velocity correlations

The time correlation for the particle's velocity fluctuations U' in a direction i with interval Δt is [52]:

$$R_{i,i}(\Delta t) = \frac{\langle U_i'(p,t)U_i'(p,t+\Delta t) \rangle}{\sigma_{U_i}^2} \quad (12)$$

where the variance is σ^2 and the angular brackets represent an ensemble average by all
 350 particles p and interval Δt . The correlations for the settling and transversal directions are
 shown in Fig. 10.

Overall, the particles decorrelate faster with a higher power-law index for the
 settling velocity, contrary to the result obtained by [34], but some differences must be
 observed, such as in the constitutive equation, boundary conditions, density ratio, and
 Archimedes number. The decrease in decorrelation time for shear-thinning fluids may
 occur because the particles that enter the wake of reduced viscosity will not deviate from
 the path since they would encounter regions with higher viscosity outside of it.

With the increase in the solid volume fraction, oscillations emerge in the
 correlations for the settling direction. As pointed out by Fornari et al. [19], these
 360 oscillations may be associated with the transition between a regime governed by the
 buoyancy to a regime in which lubrication and collision forces reign. The oscillations
 have greater intensity for a shear-thickening fluid because when two particles are
 approaching each other, the fluid viscosity increases in the gap, and so do the lubrication
 forces.

There is a moderate anti-correlation in the transversal direction for short periods
 that may be associated with particle collisions. Since the particles have the same inertia,
 and the collision is mainly elastic ($e = 0.9$), they change direction after lateral collisions.
 The magnitude of the anti-correlation increases with the power-law index, indicating that
 the intensity of collisions reduces with n . The decorrelation time reduces with the solid
 370 volume fraction, as the particles are more likely to suffer velocity fluctuations due to fluid
 perturbations.

4.3 Particle-pair statistics

In order to understand the relative position of the particles in the suspension, we utilize the pair probability distribution function that represents the probability of encountering particles in specific positions. We analyze it based on the radial and relative vertical distances, transformed to the polar angle ψ in spherical coordinates. The pair probability distribution function is given by [53]:

$$g(r, \psi) = \frac{\rho(r, \psi)}{\rho_0} = \frac{n(r, \psi)}{2\pi r^2 \sin \psi dr d\psi_s} \frac{1}{(N/V)t_s} \quad (13)$$

where the number of particles in the spherical volume is binned in a histogram $n(r, \psi)$ with
380 a bin size dr in the radial direction and $d\psi$ in the polar direction; in this work, we make $dr = 1/D$ and $d\psi = 1^\circ$. The distribution is then normalized by the average particle density of the volume analyzed (ρ_0). Values of $g(r, \psi)$ higher than 1 indicate a concentration superior to the fluid average, while values lower than 1 mean the opposite. The gravity direction is parallel to $0^\circ - 180^\circ$.

The pair probability distribution function for a solid volume fraction of $\phi = 0.2\%$ is shown in Fig. 11, where the DKT pattern can be seen for the Newtonian fluid by the high-distribution spots. Away from the particle in the equatorial plane ($\theta = 90^\circ$), there is a reduced particle concentration, as reported in previous studies [25,26,34,54]. The particle concentration increases at a distance of $3D$, which was also reported. In the shear-
390 thickening case, something unusual occurs: the particles in vertical alignment rarely collide but rather diverge before impact due to the fluid “thickening” in the gap between the two particles, also illustrated in Fig. 14.a, in an instantaneous viscosity field taken just before the collision. Instead of colliding, the trailing particle deflects at the symmetry angle of $\psi = 45^\circ$. The trajectory change is accompanied by an increased rotation, which was previously indicated by Fig. 9.a.

For the power-law index $n = 0.75$, Fig. 11.c shows that when the trailing particle is below a certain distance from the leading one, it will be attracted by the wake of reduced viscosity [12,55], shown in Fig. 15, which can be inferred from the high particle concentration can infer this at $\psi = 15^\circ$ and 165° . Similar to the Newtonian case, a particle concentration reduction occurs in the radial distances from $1.5D$ to $3D$, and an increase for distances greater than $3D$. Even though the Archimedes number is the same for all fluids, the terminal Reynolds number changes with n . Thus, particles in a lower n fluid display some inertial motion features. For example, a particle crossing the wake of reduced viscosity in an $n = 0.75$ fluid gets trapped inside the wake since it does not have enough inertia to surpass the higher viscosity fluid outside of it, while for an $n = 0.6$ fluid, it is easier to go across the wake, explaining why the zone $1.5D$ to $3D$ is more crowded when $n = 0.6$. However, there is still a high concentration zone in the equatorial plane, indicating that side-by-side settling remains frequent.

With the particle volume fraction to $\phi = 1.0\%$, some changes are observed in the pair probability distribution function, Fig. 12. There is an indication that particles preferably settle side-by-side at a distance of approximately $3D$ for $n = 1.25$, reducing to $2.5D$ for Newtonian fluid and even shorter for the shear-thinning fluids. Differently from $n = 0.75$, with $n = 0.60$, some particles settle side-by-side with contact, as shown by the high concentration at a distance $1D$, mainly due to the low viscosity of their gaps, Fig. 14.b. Another effect caused by the power-law index is the relative elevation difference when settling side-by-side. For $n = 1.25$, the concentration peak is located at $\pm 1.5D$ from the equatorial plane, increasing to $\pm 2D$ for a Newtonian fluid while maintaining the same radial distance. When the is shear-thinning, the radial distance increases compared to the Newtonian and shear-thickening cases.

420 For $\phi = 3.3\%$, depicted in Fig. 13, the magnitude of the concentration peaks are lower because the collisions frequency is higher [19,56], and therefore the particles do not stay long periods settling unobstructed. The effect of the wake of reduced viscosity is no longer visible since the collisions could expel particles out of it. Besides, the overall reduction in the fluid viscosity also diminishes its effect. In the case $n = 0.6$, the side-by-side settling with contact was enhanced with a solid volume fraction of 3.3% compared with the concentration of $\phi = 1\%$, explaining the reduction in the maximum angular velocity achieved by the particles when the power-law index decreases, Fig. 9.a-c. The reduction in the maximum angular velocity with n is not perceived for $\phi = 0.2\%$ because most particles do not settle side-by-side while being in contact.

430 4.4 Particle-average viscosity field

The ensemble-averaged viscosity field around the particles is shown in Fig. 15. In the case of a shear-thickening fluid, the average viscosity rises near the particle's surface due to the high shear rate around it. By increasing the solid-volume fraction from 0.2% to 3.3%, the average viscosity increases by approximately 50%. The average viscosity near the particle's surface does not change significantly in the concentration range analyzed. As ϕ increases, the average viscosity field becomes more uniform.

The shear-thinning average viscosity fields reveal a very high viscosity in locations away from the particle's surface. Also, the wake of reduced viscosity is very well delineated. Interestingly, the peak viscosity for $n = 0.75$ takes place in a vertical stripe
440 next to the wake and not in the far-field, as for $n = 0.6$. Consequently, the intensity of the capture effect of the wake is magnified, which was perceived in the particle-pair distribution function. The shear-thinning effect also contributes to increasing the

frequency of side-by-side settling since the particles meet a higher fluid resistance to separate from each other.

The far-field viscosity is lower by increasing the solid volume fraction in the shear-thinning fluid. Consequently, the shear-thinning effect becomes less important, and the particle collisions play a predominant role. Fig. 13 depicts the particle density homogenization in the far-field. The collisions (DKT) constantly change the particle's direction, making the viscosity field more uniform. Hence, the suspension tends to behave
450 closer to a Newtonian fluid [29].

5. CONCLUSION

This paper analyzed the effects of shear-thinning and shear-thickening fluid behaviors in the multiple particle settling of a dilute monodisperse suspension. The results were obtained through fully-resolved numerical simulations with the lattice Boltzmann method, which allowed us to obtain crucial statistical data, such as particle velocity distribution function, particle-pair distribution density, and particle-average viscosity field.

For all cases analyzed, solid volume fractions between 0.2% and 3.3% and power-law indexes between $n = 1.25$ and 0.6, it was observed hindered settling, which means
460 that the mean particle velocity was inferior to the settling rate of one particle in a quiescent fluid, with the magnitude of the hindering increasing with the solid volume fraction. Additionally, the solid volume fraction plays a crucial role in the magnitude of the particle's transversal velocity and, consequently, collisions and fluid fluctuations.

In conjunction with the viscosity field, the particle-pair distribution function allowed us to understand how the spatial distribution of particles in the suspension affects the fluid response and vice-versa. For a shear-thickening fluid, viscosity increases in the gap when the particles approach each other, preventing particle contact. On the other hand, for shear-thinning fluids, a wake of reduced viscosity attracts particles and enables
470 the draft-kissing-tumbling (DKT) process.

The increase in the solid volume fraction caused a transition of the settling regime from viscous-dominated, with preferential trajectories and a heterogeneous viscosity field, to a collision-dominated, with varied trajectories and a more uniform viscosity field. The uniformity caused the wake of reduced viscosity to have a diminished effect on the particle movement since they would not be easily captured. However, when this uniformity was not observed in low solid volume fractions, the corridor was able to

redirect the particle trajectories, leading to collisions. The draft-kissing-tumbling process still occurred in shear-thinning fluids, with the power-law index influencing the distance between the particles when they settle side-by-side.

480 For future works, we recommend the analysis of the particle's friction coefficient since the DKT process plays an essential role in the multiple particle settling. We are currently undertaking efforts to extend the present results for a broader range of density ratios and Archimedes numbers and to study the hindered settling of polydisperse shear-thinning suspensions. As a final remark, we point out that the numerical characterization of industrial suspensions is increasingly becoming possible with advances in rheology, numerical methods, and high-performance computing. We believe that many industries will benefit from this type of technology in a few years to complement experimental tests.

ACKNOWLEDGMENTS

490 The authors acknowledge the financial support of the Brazilian Coordination for the Improvement of Higher Education Personnel (CAPES), Finance Code 001. We also thank Waine Barbosa de Oliveira Junior and Luiz Gustavo Galerani Ricardo for sharing their knowledge of the software and hardware.

APPENDIX A – NUMERICAL METHOD

The LBM is a computational method that solves fluid flow in the mesoscopic scale, i.e., the collective behavior of a group of particles based on Boltzmann kinetic theory [57], instead of the mass and momentum transport equations directly. In the LBM, these groups of particles, often called populations, travel through fixed positions in space, 500 denominated lattices, and through delimited directions defined by the velocity sets. Different methods were proposed to solve this process; in the current, we used the lattice Boltzmann method with regularization of ghost moments [58–60] and with the BGK collision operator [61], used in previous works for viscoplastic fluids [10,60].

The lattice Boltzmann equation is [59,60]:

$$f_i(\mathbf{x} + \mathbf{c}_i \Delta t, t + \Delta t) = (1 - \omega) f_i^{reg}(\mathbf{x}, t) + \omega f_i^{eq}(\mathbf{x}, t) + \left(1 - \frac{\omega}{2}\right) F_i(\mathbf{x}, t) \Delta t \quad (14)$$

where f_i is the particle distribution function in the velocity direction i , and ω is the relaxation frequency. The pre-collision regularized distribution function (f^{reg}), equilibrium distribution function (f^{eq}), and discrete-velocity force term F_i are defined as [60,62,63]:

$$f^{reg} = f^{eq} + \frac{w_i}{2c_s^4} \left[(c_{i\alpha} c_{i\beta} - c_s^2 \delta_{\alpha\beta}) \sum (f_i - f_i^{eq}) c_{i\alpha} c_{i\beta} - \Delta t c_s^2 c_{i\alpha} F_\alpha \right] \quad (15)$$

$$f_i^{eq} = w_i \rho \left[1 + \frac{c_{i\alpha} u_\alpha}{c_s^2} + \frac{u_\alpha u_\beta (c_{i\alpha} c_{i\beta} - c_s^2 \delta_{\alpha\beta})}{2c_s^4} \right] \quad (16)$$

$$F_i = w_i \left[\frac{c_{i\alpha}}{c_s^2} + \frac{(c_{i\alpha} c_{i\beta} - c_s^2 \delta_{\alpha\beta}) u_\beta}{c_s^4} \right] F_\alpha \quad (17)$$

Equations (15) - (17) depend on the fluid velocity (u_α) and its density (ρ) values. These macroscopic variables can be determined as a function of the particle distribution function [59]:

$$\rho = \sum_i f_i + \frac{\Delta t}{2} \sum_i F_i \quad (18)$$

$$\rho u_\alpha = \sum_i f_i c_{i\alpha} + \frac{\Delta t}{2} \sum_i F_i c_{i\alpha} \quad (19)$$

$$\tau_{\alpha\beta} = -\left(1 - \frac{\omega}{2}\right) \left[\sum_i (f_i - f_i^{eq}) c_{i\alpha} c_{i\beta} + \frac{\Delta t}{2} \sum_i F_i c_{i\alpha} c_{i\beta} \right] = -\left(1 - \frac{\omega}{2}\right) T_{\alpha\beta} \quad (20)$$

Eq. (20) gives the local stress value. Equations (14) to (20) apply to a chosen velocity set, which has a defined set of weights (w_i), sound speed (c_s), and velocity vectors (\mathbf{c}_i). In the current work, we used the D3Q19 velocity set, which has the following values:

$$\begin{cases} c_s = 1/\sqrt{3} \\ w_i = 1/3 & , \mathbf{c}_i = (0,0,0) & , i = 0 \\ w_i = 1/18 & , \mathbf{c}_i = (\pm 1, 0, 0)(0, \pm 1, 0)(0, 0, \pm 1) & , i = 1, \dots, 6 \\ w_i = 1/36 & , \mathbf{c}_i = (\pm 1, \pm 1, 0)(\pm 1, 0, \pm 1)(0, \pm 1, \pm 1) & , i = 7, \dots, 18 \end{cases} \quad (21)$$

The lattice Boltzmann equation recovers the mass and momentum balance equations when the relaxation frequency and viscosity are related as [59,60]:

$$\eta = \rho c_s^2 \Delta t \left(\frac{1}{\omega} - \frac{1}{2} \right) \quad (22)$$

In [10], we studied a thixo-viscoplastic material similar to a Bingham material. We showed that it was possible to obtain an explicit solution for ω as a function of $T_{\alpha\beta}$ (Eq.(20)). Using the Power-law fluid constitutive equation (Eq.(3)), the same reasoning is applied to obtain the following equation:

$$\frac{K}{(\rho c_s^2)^n} \|T\|^n \omega^n + \frac{\|T\|}{2} \omega - \|T\| = 0 \quad (23)$$

which is valid for the range of $0 < \omega < 2$, which corresponds to $\infty > \eta > 0$. To solve Eq.(23) for ω , it is necessary to use some iterative process. In this work, we opted to solve Eq.(23)

using the Newton–Raphson method with ω from the previous time-step as the starting point.

We used the immersed boundary method (IBM) to solve the particle dynamics, which has its origin in Peskin’s work [64]. The no-slip condition is satisfied between the Lagrangian nodes and Eulerian nodes according to [65]:

$$\mathbf{u}^L = \sum_{\Omega} \mathbf{u}^{E,noF} \delta(\mathbf{x} - \mathbf{X}) h^3 + \sum_{\Omega} \left[\sum_{\Gamma} \frac{\Delta t}{2\rho} \mathbf{F}^L \delta(\mathbf{x} - \mathbf{X}) \Delta S \right] \delta(\mathbf{x} - \mathbf{X}) h^3 \quad (24)$$

540 where the velocity \mathbf{u}^L of the Lagrangian node depends on the unforced Eulerian velocity $\mathbf{u}^{E,noF}$ and the force \mathbf{F}^L imposed by Lagrangian nodes with surface area ΔS . The force is distributed based on the smoothed Dirac delta function, which is defined by the 4-point kernel ϕ_4 [66]:

$$\delta(\mathbf{x} - \mathbf{X}) = \frac{1}{h^3} \phi\left(\frac{x_1 - X_1}{h}\right) \phi\left(\frac{x_2 - X_2}{h}\right) \phi\left(\frac{x_3 - X_3}{h}\right) \quad (25)$$

$$\phi(r) = \begin{cases} \frac{1}{8} \left(3 - 2|r| + \sqrt{1 + 4|r| - 4|r|^2} \right) & 0 \leq |r| \leq 1 \\ \frac{1}{8} \left(5 - 2|r| - \sqrt{-7 + 12|r| - 4|r|^2} \right) & 1 < |r| \leq 2 \\ 0 & 2 < |r| \end{cases} \quad (26)$$

The equation system formed by Eq (24) is solved by an iterative method [67]. The particle motion equations, Eqs. (4) and (5) were discretized according to Feng and Michaelides rigid body approximation [68]:

$$\mathbf{U}_p^{t+1} = \left(1 + \frac{\rho_f}{\rho_p} \right) \mathbf{U}_p^t - \frac{\rho_f}{\rho_p} \mathbf{U}_p^{t-1} + \frac{1}{m_p} \left[- \sum_{L_p} \mathbf{F}^L \Delta S + (m_p - m_f) \mathbf{g} \right] \Delta t \quad (27)$$

550

$$\boldsymbol{\omega}_p^{t+1} = \left(1 + \frac{\rho_f}{\rho_p} \right) \boldsymbol{\omega}_p^t - \frac{\rho_f}{\rho_p} \boldsymbol{\omega}_p^{t-1} + \mathbf{I}_p^{-1} \left[- \sum_{L_p} (\mathbf{X}^t - \mathbf{X}_p^t) \times \mathbf{F}^L \Delta S \right] \Delta t \quad (28)$$

$$\mathbf{X}_p^{t+1} = \mathbf{X}_p^t + \frac{\mathbf{U}_p^{t+1} + \mathbf{U}_p^t}{2} \Delta t \quad (29)$$

In the current work, we study the settling of multiple particles. One cannot guarantee that triple collisions will not occur in such a case. Therefore, we opted to use a soft-sphere collision model. To model the particle-particle collisions as well as the particle-wall, we used a Hertzian contact model in which the normal collision force is given by a spring dash-pot system [37]:

$$\mathbf{F}_{n,ij} = -\left(k_n \delta_n^{3/2} + D_{n,j} \mathbf{U}_r \cdot \hat{\mathbf{n}}\right) \hat{\mathbf{n}} \quad (30)$$

where k_n is the normal stiffness coefficient, δ_n is the normal displacement, D_n is the normal damping coefficient, and \mathbf{U}_r is the relative velocity between the element i and j .

560 The normal stiffness coefficient is found based on the material's mechanical properties and the radius in the contact region (r) [69,70]:

$$k_n = \frac{4}{3} \left(\frac{1-\nu_i^2}{E_i} + \frac{1-\nu_j^2}{E_j} \right)^{-1} \left(\frac{r_i + r_j}{r_i r_j} \right)^{-1/2} \quad (31)$$

where E is Young's modulus, and ν is the Poisson ratio. The tangential force acting in the particles during the collision is:

$$\mathbf{F}_{t,ij} = -\left(k_t \delta_t + D_{t,j} \mathbf{U}_r \cdot \hat{\mathbf{t}}\right) \hat{\mathbf{t}} \quad (32)$$

where k_t is the tangential stiffness coefficient defined as a function of the shear modulus G and the equivalent contact radius a [37,71]:

$$k_t = 8a \left(\frac{2-\nu_i}{G_i} + \frac{2-\nu_j}{G_j} \right)^{-1} \quad (33)$$

One of the most commonly measured mechanical properties of particles is the
570 restitution coefficient e . It can translate to the damping coefficient as [37,72]:

$$D = -\frac{2 \ln e}{\sqrt{\pi^2 + \ln^2(e)}} \delta^{1/4} \sqrt{m_{eq} k} \quad (34)$$

where m_{eq} is the equivalent mass of the system, k is the respective stiffness coefficient, and δ is the displacement/penetration distance. The friction coefficient μ defines if the particle will roll or slide. If $F_{t,ij} > fF_{n,ij}$, the tangential force is given by

$$F_{t,ij} = \mu F_{n,ij} \cdot \mathbf{t} \quad (35)$$

When particles approach too close, hydrodynamic forces appear due to the fluid being squeezed between the surface of the particles (lubrication force). When the spatial discretization is not fine enough, the lubrication force will not be correctly represented. For practical reasons, some solvers often implement it separately. When implemented for
 580 a Newtonian fluid, the lubrication force between two spherical particles is approximated as $F_L = 1.5\pi\mu R^2 U/h$ [46,73] for a Newtonian fluid. However, for non-Newtonian fluids, its formulation is significantly more complex [74–78], if any solution is possible at all [74]. A peculiar issue arises due to the grid resolution employed in this work: the lubrication force is partially evaluated. In other words, the method can predict the force up to a certain gap, and below that, it underestimates the lubrication force. The validation test of Sec. 3.3 was used to analyze the need to incorporate a model for the lubrication force. It was observed that the addition of a lubrication model [46] did not significantly improve the numerical outcome. The lubrication force is relevant in a small interval. So, in the case tested, no significant velocity change took place

590

6. REFERENCES

- [1] H.P. Zhu, Z.Y. Zhou, R.Y. Yang, A.B. Yu, Discrete particle simulation of particulate systems: A review of major applications and findings, *Chem. Eng. Sci.* 63 (2008) 5728–5770. <https://doi.org/10.1016/j.ces.2008.08.006>.
- [2] G.G. Stokes, On the Effect of the Internal Friction of Fluids on the Motion of Pendulums, in: *Trans. Cambridge Philos. Soc.*, Cambridge University Press, Cambridge, 1850: pp. 8–106. <https://archive.org/details/transactionsofca09camb/page/8>.
- 600 [3] M. Jenny, J. Duek, G. Bouchet, Instabilities and transition of a sphere falling or ascending freely in a Newtonian fluid, *J. Fluid Mech.* 508 (2004) 201–239. <https://doi.org/10.1017/S0022112004009164>.
- [4] M. Horowitz, C.H.K. Williamson, The effect of Reynolds number on the dynamics and wakes of freely rising and falling spheres, *J. Fluid Mech.* 651 (2010) 251–294. <https://doi.org/10.1017/S0022112009993934>.
- [5] W. Zhou, J. Dušek, Chaotic states and order in the chaos of the paths of freely falling and ascending spheres, *Int. J. Multiph. Flow.* 75 (2015) 205–223. <https://doi.org/10.1016/j.ijmultiphaseflow.2015.05.010>.
- [6] F. Auguste, J. Magnaudet, Path oscillations and enhanced drag of light rising spheres, *J. Fluid Mech.* 841 (2018) 228–266. <https://doi.org/10.1017/jfm.2018.100>.
- 610 [7] R.W. Ansley, T.N. Smith, Motion of spherical particles in a Bingham plastic, *AIChE J.* 13 (1967) 1193–1196. <https://doi.org/10.1002/aic.690130629>.
- [8] M.J. King, N.D. Waters, The unsteady motion of a sphere in an elastico-viscous liquid, *J. Phys. D. Appl. Phys.* 5 (1972) 318. <https://doi.org/10.1088/0022->

3727/5/1/318.

- [9] R.P. Chhabra, A.A. Soares, J.M. Ferreira, A numerical study of the accelerating motion of a dense rigid sphere in non-newtonian power law fluids, *Can. J. Chem. Eng.* 76 (1998) 1051–1055. <https://doi.org/10.1002/cjce.5450760611>.
- 620 [10] M.A. Ferrari, A. Lugarini, A.T. Franco, Fully-resolved simulations of a sphere settling in an initially unstructured thixo-viscoplastic fluid, *J. Nonnewton. Fluid Mech.* 294 (2021) 104574. <https://doi.org/10.1016/j.jnnfm.2021.104574>.
- [11] A.F. Fortes, D.D. Joseph, T.S. Lundgren, Nonlinear mechanics of fluidization of beds of spherical particles, *J. Fluid Mech.* 177 (1987) 467–483. <https://doi.org/10.1017/S0022112087001046>.
- [12] S. Daugan, L. Talini, B. Herzhaft, C. Allain, Aggregation of particles settling in shear-thinning fluids, *Eur. Phys. J. E.* 7 (2002) 73–81. <https://doi.org/10.1140/epje/i200101116>.
- [13] A.H. Sulaymon, C.A.M.E. Wilson, A.I. Alwared, An experimental investigation of the settling behavior of two spheres in a power-law fluid, *J. Nonnewton. Fluid Mech.* 192 (2013) 29–36. <https://doi.org/10.1016/j.jnnfm.2012.09.011>.
- 630 [14] T.-W. Pan, R. Glowinski, Numerical study of spheres settling in Oldroyd-B fluids, *Phys. Fluids.* 30 (2018) 113102. <https://doi.org/10.1063/1.5032324>.
- [15] M.J. Riddle, C. Narvaez, R.B. Bird, Interactions between two spheres falling along their line of centers in a viscoelastic fluid, *J. Nonnewton. Fluid Mech.* 2 (1977) 23–35. [https://doi.org/10.1016/0377-0257\(77\)80030-X](https://doi.org/10.1016/0377-0257(77)80030-X).
- [16] Z. Qi, S. Kuang, L. Rong, A. Yu, Lattice Boltzmann investigation of the wake effect on the interaction between particle and power-law fluid flow, *Powder Technol.* 326 (2018) 208–221. <https://doi.org/10.1016/j.powtec.2017.12.015>.
- 640 [17] W.K. Lewis, E.R. Gilliland, W.C. Bauer, Characteristics of Fluidized Particles,

- Ind. Eng. Chem. 41 (1949) 1104–1117. <https://doi.org/10.1021/ie50474a004>.
- [18] E.M. Tory, M.T. Kamel, C.F.C.M. Fong, Sedimentation is container-size dependent, *Powder Technol.* 73 (1992) 219–238. [https://doi.org/10.1016/0032-5910\(92\)85029-U](https://doi.org/10.1016/0032-5910(92)85029-U).
- [19] W. Fornari, S. Zade, L. Brandt, F. Picano, Settling of finite-size particles in turbulence at different volume fractions, *Acta Mech.* 230 (2019) 413–430. <https://doi.org/10.1007/s00707-018-2269-1>.
- [20] J.F. Richardson, W.N. Zaki, The sedimentation of a suspension of uniform spheres under conditions of viscous flow, *Chem. Eng. Sci.* 3 (1954) 65–73. [https://doi.org/10.1016/0009-2509\(54\)85015-9](https://doi.org/10.1016/0009-2509(54)85015-9).
- 650 [21] E. Barnea, J. Mizrahi, A generalized approach to the fluid dynamics of particulate systems, *Chem. Eng. J.* 5 (1973) 171–189. [https://doi.org/10.1016/0300-9467\(73\)80008-5](https://doi.org/10.1016/0300-9467(73)80008-5).
- [22] R. Johne, Einfluß der Konzentration einer monodispersen Suspension auf die Sinkgeschwindigkeit ihrer Teilchen, *Chemie Ing. Tech.* 38 (1966) 428–430. <https://doi.org/10.1002/cite.330380407>.
- [23] B. Koglin, Statistische Verteilung der Sedimentationsgeschwindigkeit in niedrig konzentrierten Suspensionen, *Chemie Ing. Tech. - CIT.* 43 (1971) 761–764. <https://doi.org/10.1002/cite.330431306>.
- 660 [24] X. Yin, D.L. Koch, Hindered settling velocity and microstructure in suspensions of solid spheres with moderate Reynolds numbers, *Phys. Fluids.* 19 (2007) 1–16. <https://doi.org/10.1063/1.2764109>.
- [25] M. Uhlmann, T. Doychev, Sedimentation of a dilute suspension of rigid spheres at intermediate Galileo numbers: the effect of clustering upon the particle motion, *J. Fluid Mech.* 752 (2014) 310–348. <https://doi.org/10.1017/jfm.2014.330>.

- [26] T. Shajahan, W.P. Breugem, Influence of Concentration on Sedimentation of a Dense Suspension in a Viscous Fluid, *Flow, Turbul. Combust.* 105 (2020) 537–554. <https://doi.org/10.1007/s10494-020-00172-8>.
- [27] S.G. Huisman, T. Barois, M. Bourgoïn, A. Chouippe, T. Doychev, P. Huck, C.E.B. Morales, M. Uhlmann, R. Volk, Columnar structure formation of a dilute suspension of settling spherical particles in a quiescent fluid, *Phys. Rev. Fluids.* 1 (2016) 074204. <https://doi.org/10.1103/PhysRevFluids.1.074204>.
- [28] R.P. Chhabra, S.S. Peri, Simple method for the estimation of free-fall velocity of spherical particles in power law liquids, *Powder Technol.* 67 (1991) 287–290. [https://doi.org/10.1016/0032-5910\(91\)80110-5](https://doi.org/10.1016/0032-5910(91)80110-5).
- [29] R.P. Chhabra, A. Unnikrishnan, V.R.U. Nair, Hindered settling in non-newtonian power law liquids, *Can. J. Chem. Eng.* 70 (2009) 716–720. <https://doi.org/10.1002/cjce.5450700414>.
- [30] E. Allen, P.H.T. Uhlherr, Nonhomogeneous Sedimentation in Viscoelastic Fluids, *J. Rheol. (N. Y. N. Y.)* 33 (1989) 627–638. <https://doi.org/10.1122/1.550030>.
- [31] R.H. Weiland, Y.P. Fessas, B. V. Ramarao, On instabilities arising during sedimentation of two-component mixtures of solids, *J. Fluid Mech.* 142 (1984) 383–389. <https://doi.org/10.1017/S0022112084001154>.
- [32] S. Dagan, L. Talini, B. Herzhaft, Y. Peysson, C. Allain, Sedimentation of suspensions in shear-thinning fluids, *Oil Gas Sci. Technol.* 59 (2004) 71–80. <https://doi.org/10.2516/ogst:2004007>.
- [33] B.A. Moreira, F. de Oliveira Arouca, J.J.R. Damasceno, Analysis of suspension sedimentation in fluids with rheological shear-thinning properties and thixotropic effects, *Powder Technol.* 308 (2017) 290–297. <https://doi.org/10.1016/j.powtec.2016.12.034>.

- [34] D. Alghalibi, W. Fornari, M.E. Rosti, L. Brandt, Sedimentation of finite-size particles in quiescent wall-bounded shear-thinning and Newtonian fluids, *Int. J. Multiph. Flow.* 129 (2020) 103291. <https://doi.org/10.1016/j.ijmultiphaseflow.2020.103291>.
- [35] R.F. Mitchell, S.Z. Miska, *Fundamentals of Drilling Engineering*, 1st ed., Society of Petroleum Engineers, Richardson, 2011.
- [36] R.P. Chhabra, *Bubbles, Drops and Particles in Non-Newtonian Fluids*, 2nd ed., CRC Press, 2006.
- 700 [37] Y. Tsuji, T. Kawaguchi, T. Tanaka, Discrete particle simulation of two-dimensional fluidized bed, *Powder Technol.* 77 (1993) 79–87. [https://doi.org/10.1016/0032-5910\(93\)85010-7](https://doi.org/10.1016/0032-5910(93)85010-7).
- [38] A.J.C. Ladd, Numerical simulations of particulate suspensions via a discretized Boltzmann equation. Part 1. Theoretical foundation, *J. Fluid Mech.* 271 (1994) 285–309. <https://doi.org/10.1017/S0022112094001771>.
- [39] S. Gabbanelli, G. Drazer, J. Koplik, Lattice Boltzmann method for non-Newtonian (power-law) fluids, *Phys. Rev. E.* 72 (2005) 046312. <https://doi.org/10.1103/PhysRevE.72.046312>.
- 710 [40] C.-H. Wang, J.-R. Ho, A lattice Boltzmann approach for the non-Newtonian effect in the blood flow, *Comput. Math. with Appl.* 62 (2011) 75–86. <https://doi.org/10.1016/j.camwa.2011.04.051>.
- [41] D. Song, R.K. Gupta, R.P. Chhabra, Drag on a sphere in Poiseuille flow of shear-thinning power-law fluids, *Ind. Eng. Chem. Res.* 50 (2011) 13105–13115. <https://doi.org/10.1021/ie102120p>.
- [42] R. Darby, Determining Settling Rates of Particles, *Chem. Eng.* 103 (1996) 109–112.

- [43] S.N. Shah, Y. El Fadili, R.P. Chhabra, New model for single spherical particle settling velocity in power law (visco-inelastic) fluids, *Int. J. Multiph. Flow.* 33 (2007) 51–66. <https://doi.org/10.1016/j.ijmultiphaseflow.2006.06.006>.
- [44] S.D. Dhole, R.P. Chhabra, V. Eswaran, Flow of Power-Law Fluids Past a Sphere at Intermediate Reynolds Numbers, *Ind. Eng. Chem. Res.* 45 (2006) 4773–4781. <https://doi.org/10.1021/ie0512744>.
- [45] P. Gondret, M. Lance, L. Petit, Bouncing motion of spherical particles in fluids, *Phys. Fluids.* 14 (2002) 643–652. <https://doi.org/10.1063/1.1427920>.
- [46] R.H. Davis, J.-M. Serayssol, E.J. Hinch, The elastohydrodynamic collision of two spheres, *J. Fluid Mech.* 163 (1986) 479–497. <https://doi.org/10.1017/S0022112086002392>.
- [47] A.H. Kharaz, D.A. Gorham, A.D. Salman, An experimental study of the elastic rebound of spheres, *Powder Technol.* 120 (2001) 281–291. [https://doi.org/10.1016/S0032-5910\(01\)00283-2](https://doi.org/10.1016/S0032-5910(01)00283-2).
- 730 [48] N. Maw, J.R. Barber, J.N. Fawcett, The oblique impact of elastic spheres, *Wear.* 38 (1976) 101–114. [https://doi.org/10.1016/0043-1648\(76\)90201-5](https://doi.org/10.1016/0043-1648(76)90201-5).
- [49] N. Maw, J.R. Barber, J.N. Fawcett, The role of elastic tangential compliance in oblique impact., 103 (1980).
- [50] Y.C. Chung, Discrete element modelling and experimental validation of a granular solid subject to different loading conditions, The University of Edinburgh, 2006.
- [51] A. Amiri Delouei, M. Nazari, M.H. Kayhani, S.K. Kang, S. Succi, Non-Newtonian particulate flow simulation: A direct-forcing immersed boundary–lattice Boltzmann approach, *Phys. A Stat. Mech. Its Appl.* 447 (2016) 1–20. <https://doi.org/10.1016/j.physa.2015.11.032>.
- 740 [52] W. Fornari, F. Picano, L. Brandt, Sedimentation of finite-size spheres in quiescent

- and turbulent environments, *J. Fluid Mech.* 788 (2016) 640–669.
<https://doi.org/10.1017/jfm.2015.698>.
- [53] P.M. Kulkarni, J.F. Morris, Suspension properties at finite Reynolds number from simulated shear flow, *Phys. Fluids*. 20 (2008) 1–14.
<https://doi.org/10.1063/1.2911017>.
- [54] A.A. Zaidi, Particle resolved direct numerical simulation of free settling particles for the study of effects of momentum response time on drag force, *Powder Technol.* 335 (2018) 222–234. <https://doi.org/10.1016/j.powtec.2018.04.058>.
- 750 [55] Z. Yu, A. Wachs, Y. Peysson, Numerical simulation of particle sedimentation in shear-thinning fluids with a fictitious domain method, *J. Nonnewton. Fluid Mech.* 136 (2006) 126–139. <https://doi.org/10.1016/j.jnnfm.2006.03.015>.
- [56] S. Sundaram, L.R. Collins, Collision statistics in an isotropic particle-laden turbulent suspension. Part 1. Direct numerical simulations, *J. Fluid Mech.* 335 (1997) 75–109. <https://doi.org/10.1017/S0022112096004454>.
- [57] L. Boltzmann, *Vorlesungen uber Gastheorie*, Leipzig, J. A. Barth, 1896.
<https://archive.org/details/vorlesungenberg01boltgoog/page/n55/mode/2up>.
- [58] J. Latt, B. Chopard, Lattice Boltzmann method with regularized pre-collision distribution functions, *Math. Comput. Simul.* 72 (2006) 165–168.
<https://doi.org/10.1016/j.matcom.2006.05.017>.
- 760 [59] G. Silva, V. Semiao, First-and second-order forcing expansions in a lattice Boltzmann method reproducing isothermal hydrodynamics in artificial compressibility form, *J. Fluid Mech.* 698 (2012) 282–303.
<https://doi.org/10.1017/jfm.2012.83>.
- [60] A. Lugarini, A.T. Franco, P.C. Philippi, Lattice Boltzmann Method for Viscoplastic Fluid Flow Based on Regularization of Ghost Moments, *J.*

Nonnewton. Fluid Mech. 286 (2020) 104413.

<https://doi.org/10.1016/j.jnnfm.2020.104413>.

- [61] P.L. Bhatnagar, E.P. Gross, M. Krook, A Model for Collision Processes in Gases. I. Small Amplitude Processes in Charged and Neutral One-Component Systems, Phys. Rev. 94 (1954) 511–525. <https://doi.org/10.1103/PhysRev.94.511>.
- [62] Z. Guo, C. Zheng, B. Shi, Discrete lattice effects on the forcing term in the lattice Boltzmann method, Phys. Rev. E. 65 (2002) 046308. <https://doi.org/10.1103/PhysRevE.65.046308>.
- [63] X. He, L. shi Luo, Theory of the lattice Boltzmann method: From the Boltzmann equation to the lattice Boltzmann equation, Phys. Rev. E. 56 (1997) 6811–6817. <https://doi.org/10.1103/PhysRevE.56.6811>.
- [64] C.S. Peskin, Flow patterns around heart valves: A numerical method, J. Comput. Phys. 10 (1972) 252–271. [https://doi.org/10.1016/0021-9991\(72\)90065-4](https://doi.org/10.1016/0021-9991(72)90065-4).
- [65] J. Wu, C. Shu, An improved immersed boundary-lattice Boltzmann method for simulating three-dimensional incompressible flows, J. Comput. Phys. 229 (2010) 5022–5042. <https://doi.org/10.1016/j.jcp.2010.03.024>.
- [66] C.S. Peskin, The immersed boundary method, Acta Numer. 11 (2002) 479–517. <https://doi.org/10.1017/S0962492902000077>.
- [67] S.K. Kang, Y.A. Hassan, A comparative study of direct-forcing immersed boundary-lattice Boltzmann methods for stationary complex boundaries, Int. J. Numer. Methods Fluids. 66 (2011) 1132–1158. <https://doi.org/10.1002/fld.2304>.
- [68] Z.-G. Feng, E.E. Michaelides, Robust treatment of no-slip boundary condition and velocity updating for the lattice-Boltzmann simulation of particulate flows, Comput. Fluids. 38 (2009) 370–381. <https://doi.org/10.1016/j.compfluid.2008.04.013>.

- [69] H. Hertz, Über die Berührung fester elastischer Körper, *J. Für Die Reine Und Angew. Math.* 171 (1881) 156–171.
- [70] K.L. Johnson, *Contact Mechanics*, Cambridge University Press, 1985.
<https://doi.org/10.1017/CBO9781139171731>.
- [71] R.D. Mindlin, Compliance of Elastic Bodies in Contact, *J. Appl. Mech.* 16 (1949) 259–268. <https://doi.org/10.1115/1.4009973>.
- [72] Y. Tsuji, T. Tanaka, T. Ishida, Lagrangian numerical simulation of plug flow of cohesionless particles in a horizontal pipe, *Powder Technol.* 71 (1992) 239–250.
[https://doi.org/10.1016/0032-5910\(92\)88030-L](https://doi.org/10.1016/0032-5910(92)88030-L).
- 800 [73] W. Zhang, R. Noda, M. Horio, Evaluation of lubrication force on colliding particles for DEM simulation of fluidized beds, *Powder Technol.* 158 (2005) 92–101. <https://doi.org/10.1016/j.powtec.2005.04.021>.
- [74] G.J. Rodin, Squeeze film between two spheres in a power-law fluid, *J. Nonnewton. Fluid Mech.* 63 (1996) 141–152. [https://doi.org/10.1016/0377-0257\(95\)01414-4](https://doi.org/10.1016/0377-0257(95)01414-4).
- [75] G. Lian, Y. Xu, W. Huang, M.J. Adams, On the squeeze flow of a power-law fluid between rigid spheres, *J. Nonnewton. Fluid Mech.* 100 (2001) 151–164.
[https://doi.org/10.1016/S0377-0257\(01\)00140-9](https://doi.org/10.1016/S0377-0257(01)00140-9).
- [76] A. Vázquez-Quesada, M. Ellero, Analytical solution for the lubrication force between two spheres in a bi-viscous fluid, *Phys. Fluids.* 28 (2016) 073101.
810 <https://doi.org/10.1063/1.4954815>.
- [77] A.R. Koblitz, S. Lovett, N. Nikiforakis, Viscoplastic squeeze flow between two identical infinite circular cylinders, *Phys. Rev. Fluids.* 3 (2018) 023301.
<https://doi.org/10.1103/PhysRevFluids.3.023301>.
- [78] A. Vázquez-Quesada, N.J. Wagner, M. Ellero, Normal lubrication force between spherical particles immersed in a shear-thickening fluid, *Phys. Fluids.* 30 (2018)

123102. <https://doi.org/10.1063/1.5054067>.

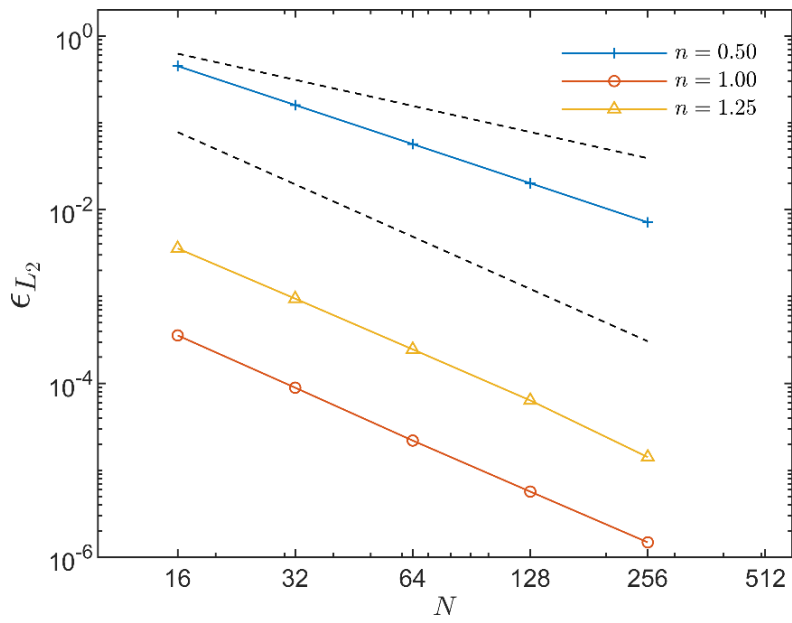


Fig. 1 - Poiseuille flow of power-law fluid. Quadratic error norm ϵ_{L_2} for the velocity profile as a function of spatial discretization N . Dashed lines represent decay orders of 1 and 2.

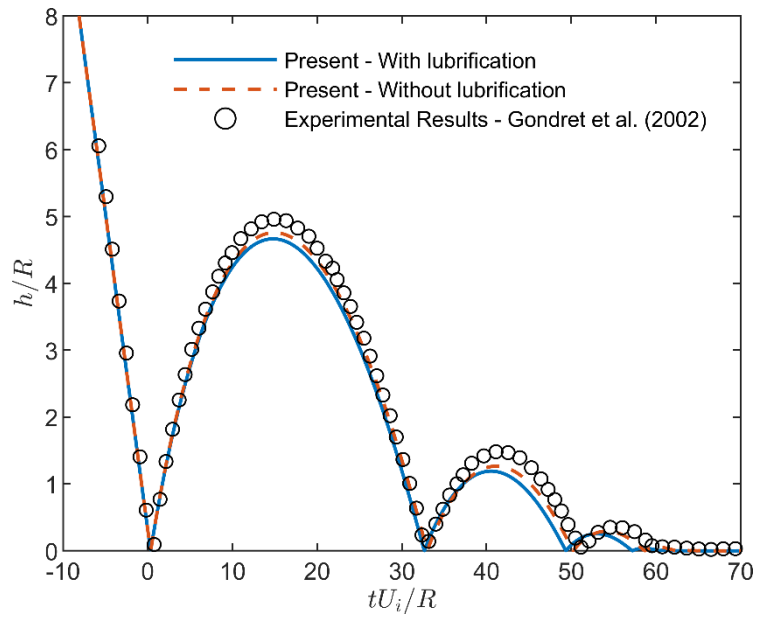
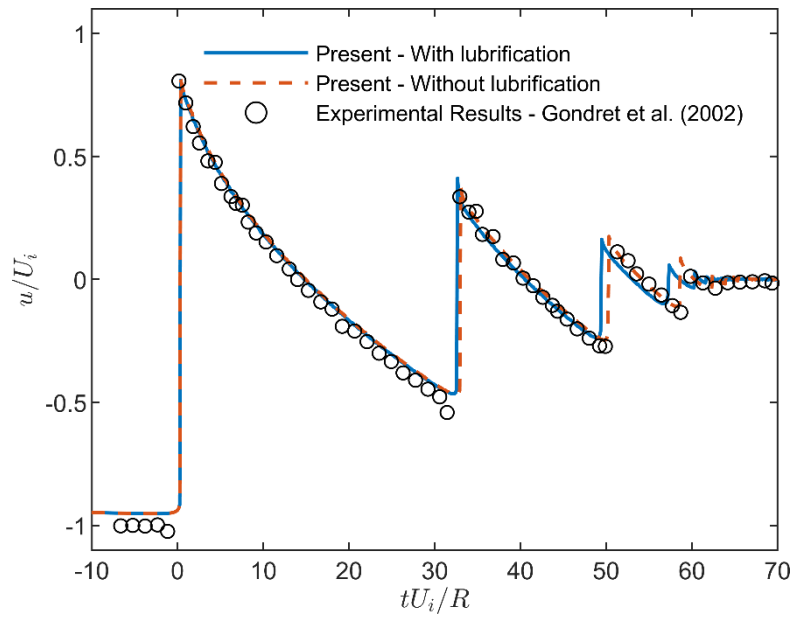


Fig. 2 - Inelastic particle rebound in a Newtonian fluid. Comparison of particle position with and without lubrication force with the experimental results of Gondret et al. [45].



830 Fig. 3 - Inelastic particle rebound in a Newtonian fluid. Comparison of particle velocity with and without lubrication force with the experimental results of Gondret et al. [45].

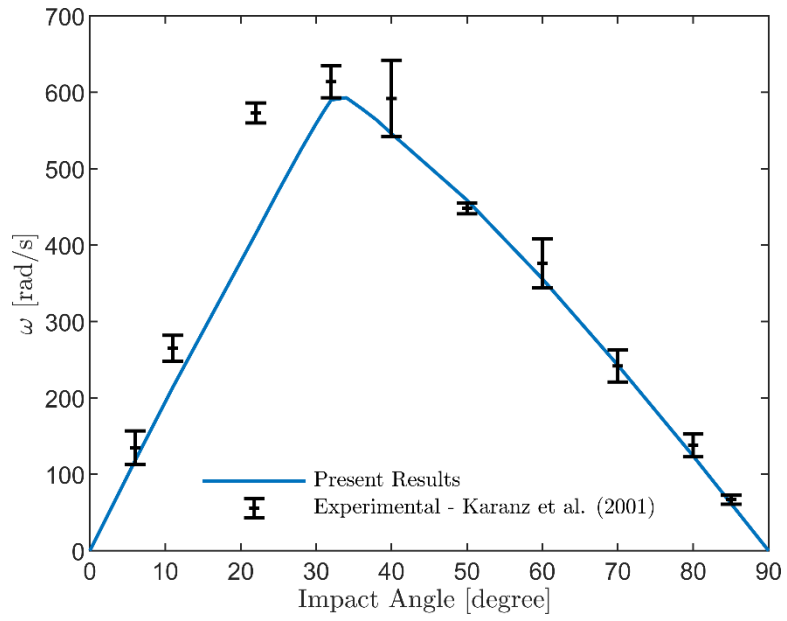


Fig. 4 - Particle collision against an inclined plane. Comparative of the numerical results and the experimental results Kharanz et al. [47] for the rotational velocity as a function of the impact angle.

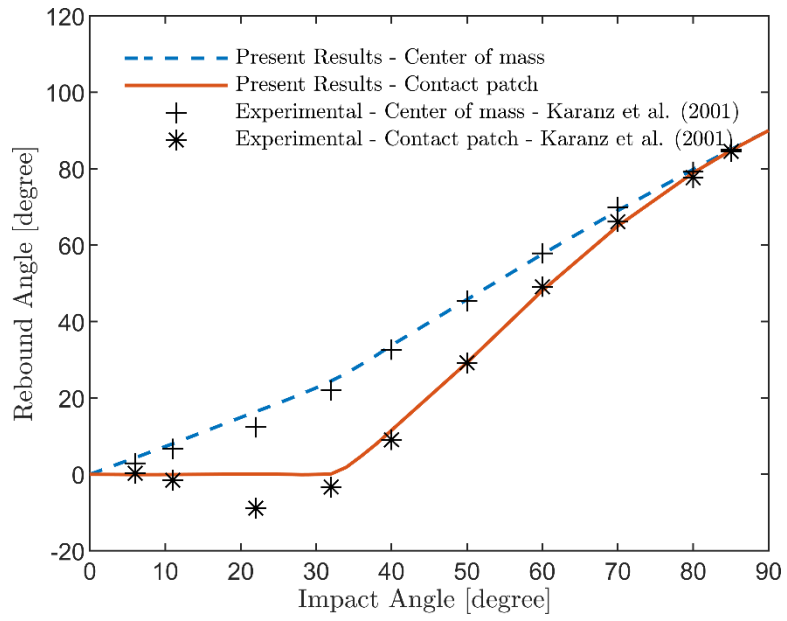


Fig. 5 - Particle collision against an inclined plane. Rebound angle of the center of mass and contact patch as a function of the impact angle. Experimental results of Kharanz et al. [47].

840

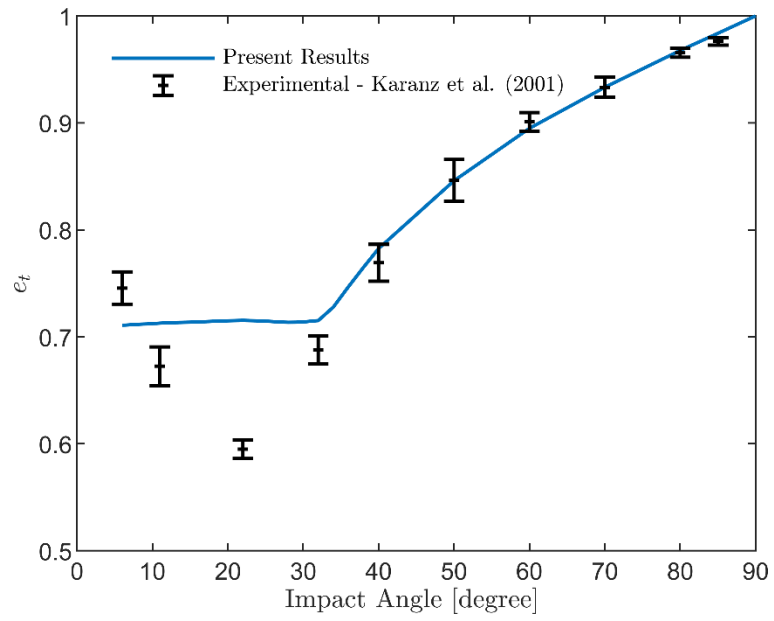


Fig. 6 - Particle collision against an inclined plane. Tangential restitution coefficient as a function of the impact angle. Experimental results of Kharanz et al. [47].

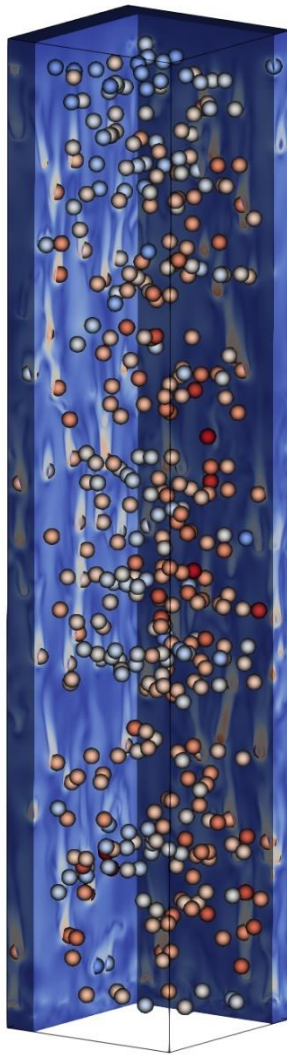


Fig. 7 – Illustration of the liquid and solid velocities with $\rho_r = 2.25$, $\phi = 3.3\%$, $Ar = 1000$, and $n = 0.6$.
(Color in print).

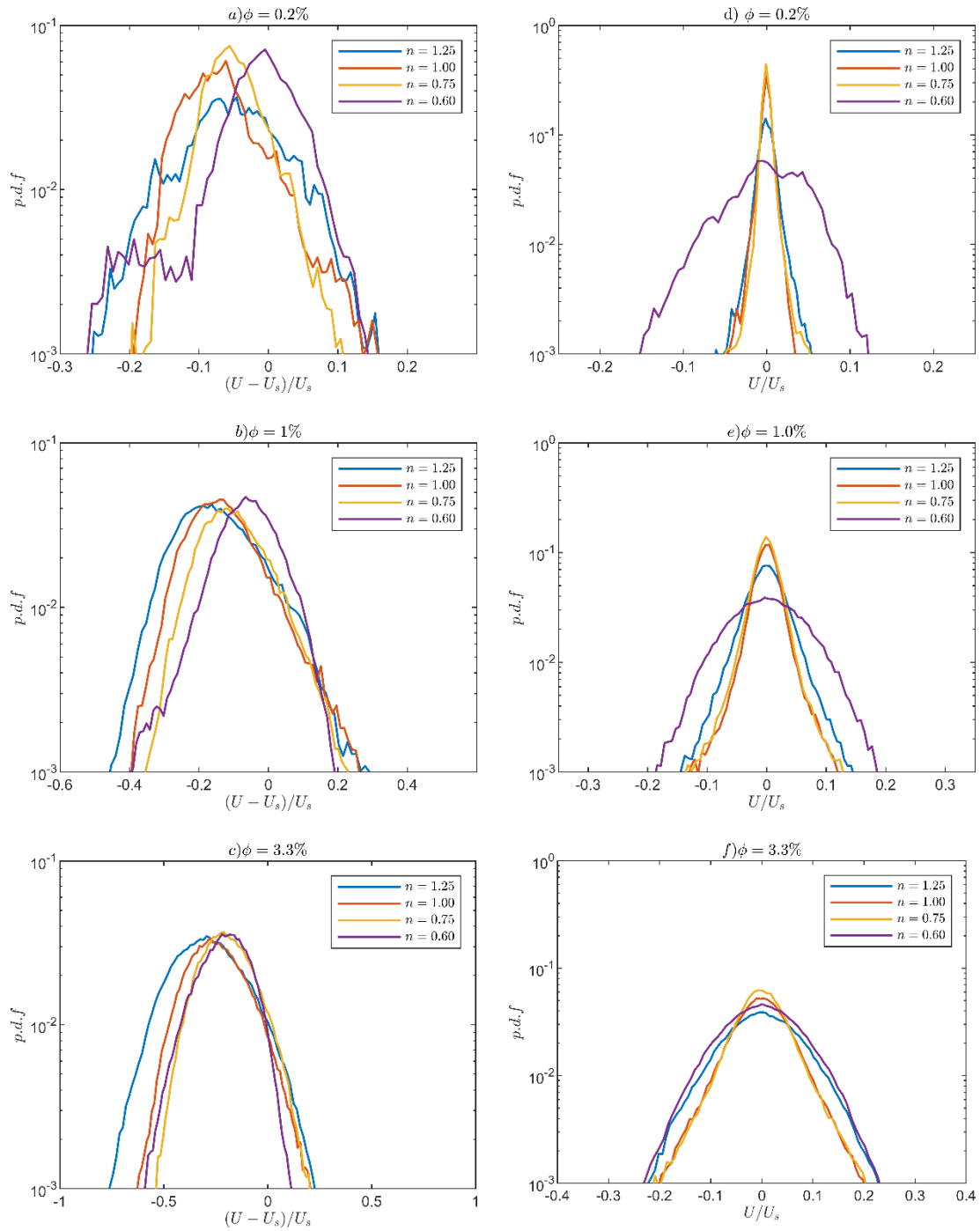


Fig. 8 - Velocity distribution functions for the settling velocity (a-c) and the lateral velocity (d-f). (Color in print).

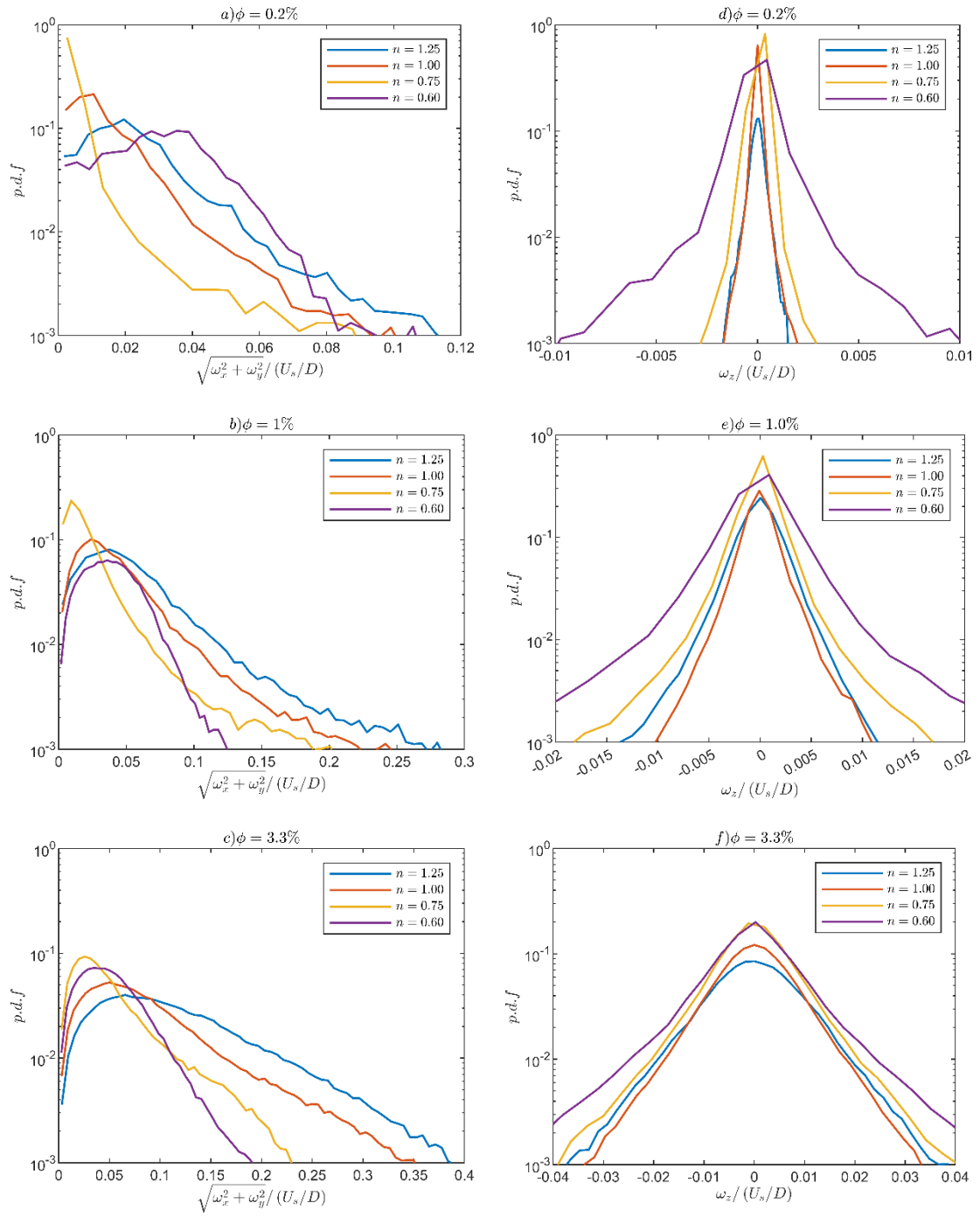


Fig. 9 - Rotational velocity distribution functions for the lateral direction (a-c) and settling direction (d-f). (Color in print).

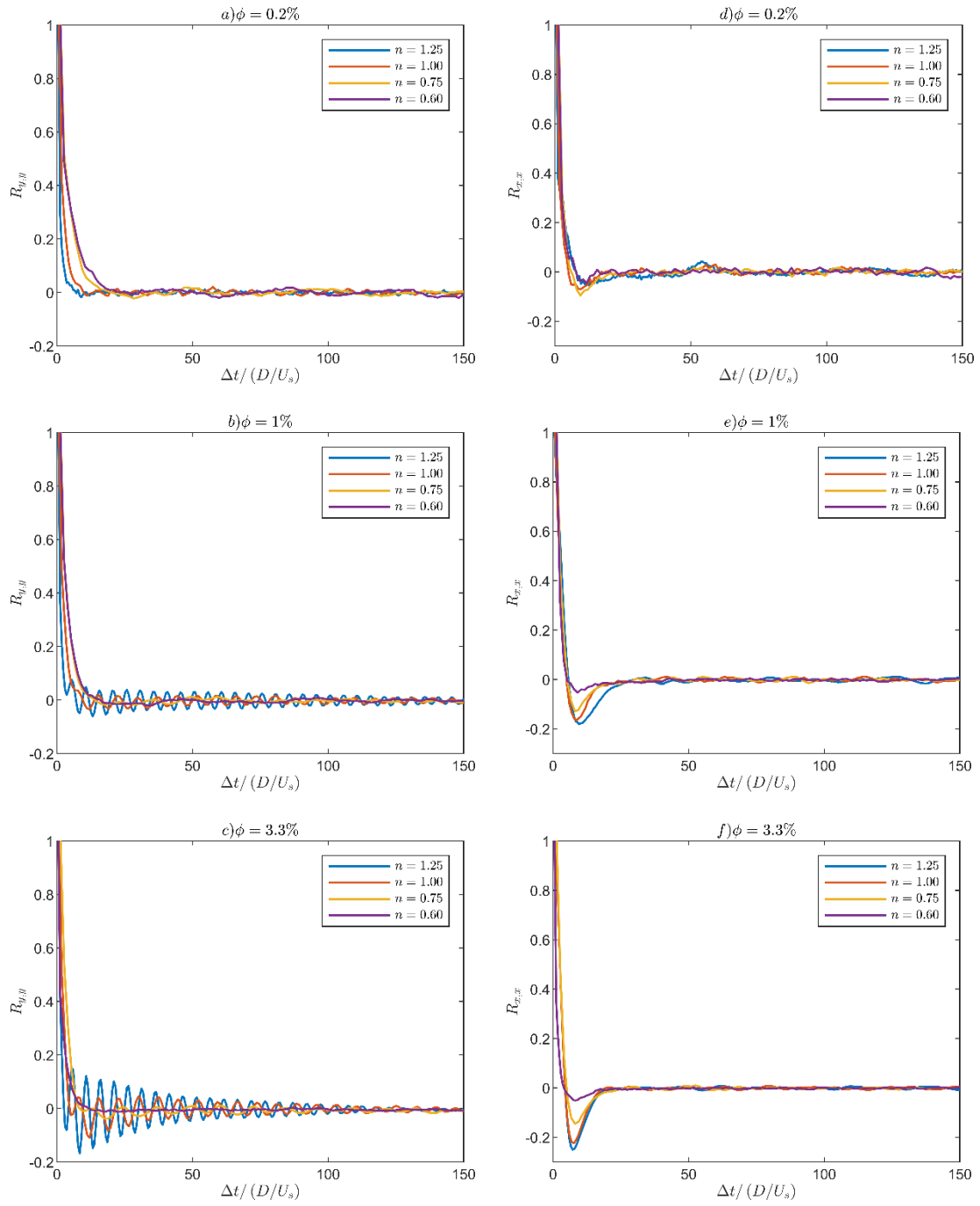


Fig. 10 – Time correlation for the particle’s velocity fluctuations. a) – c) settling direction. d) – f) transversal direction. (Color in print).

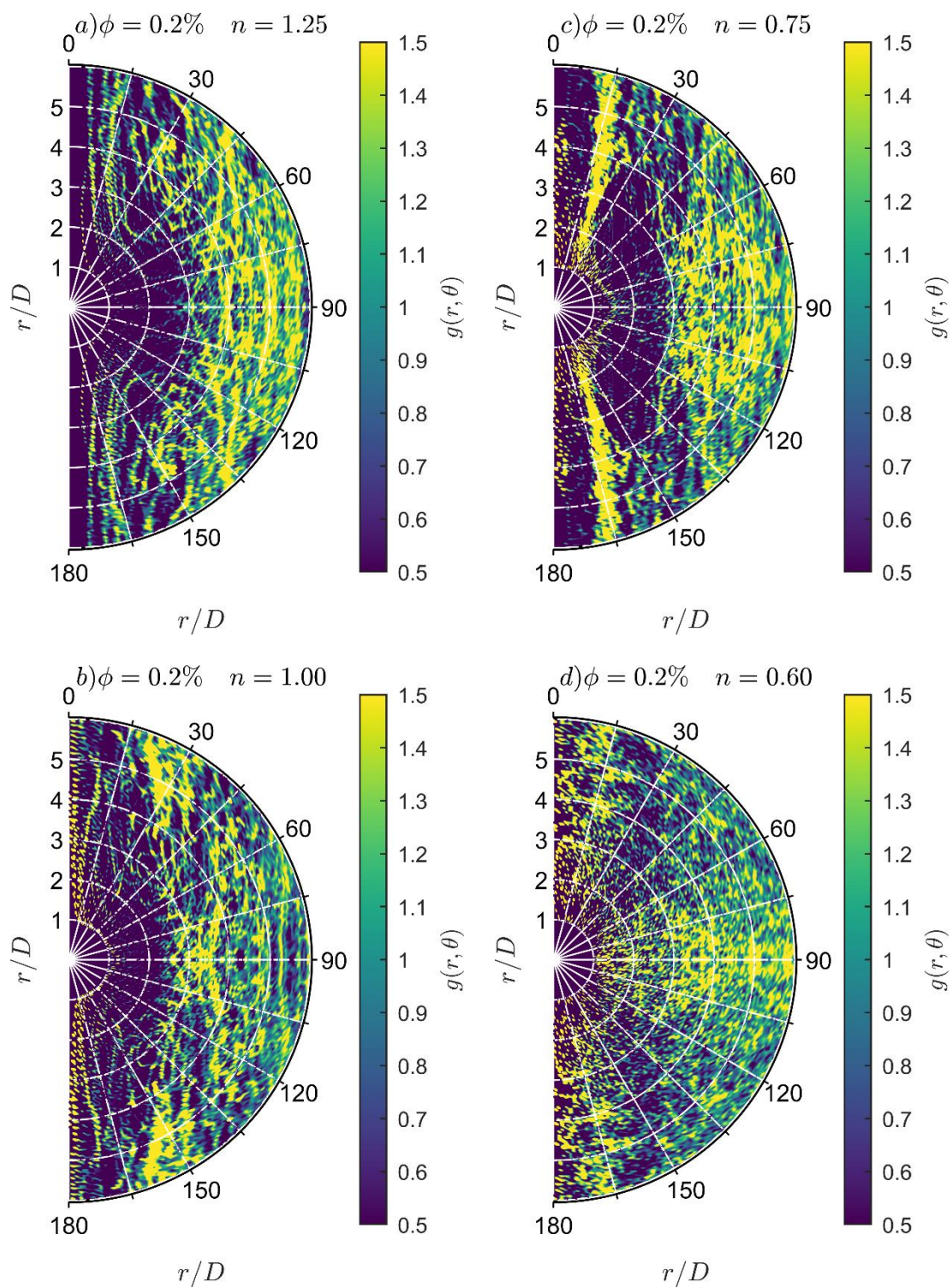


Fig. 11 –Spherical distribution function with $\phi = 0.2\%$ and $Ar = 1000$. (Color in print).

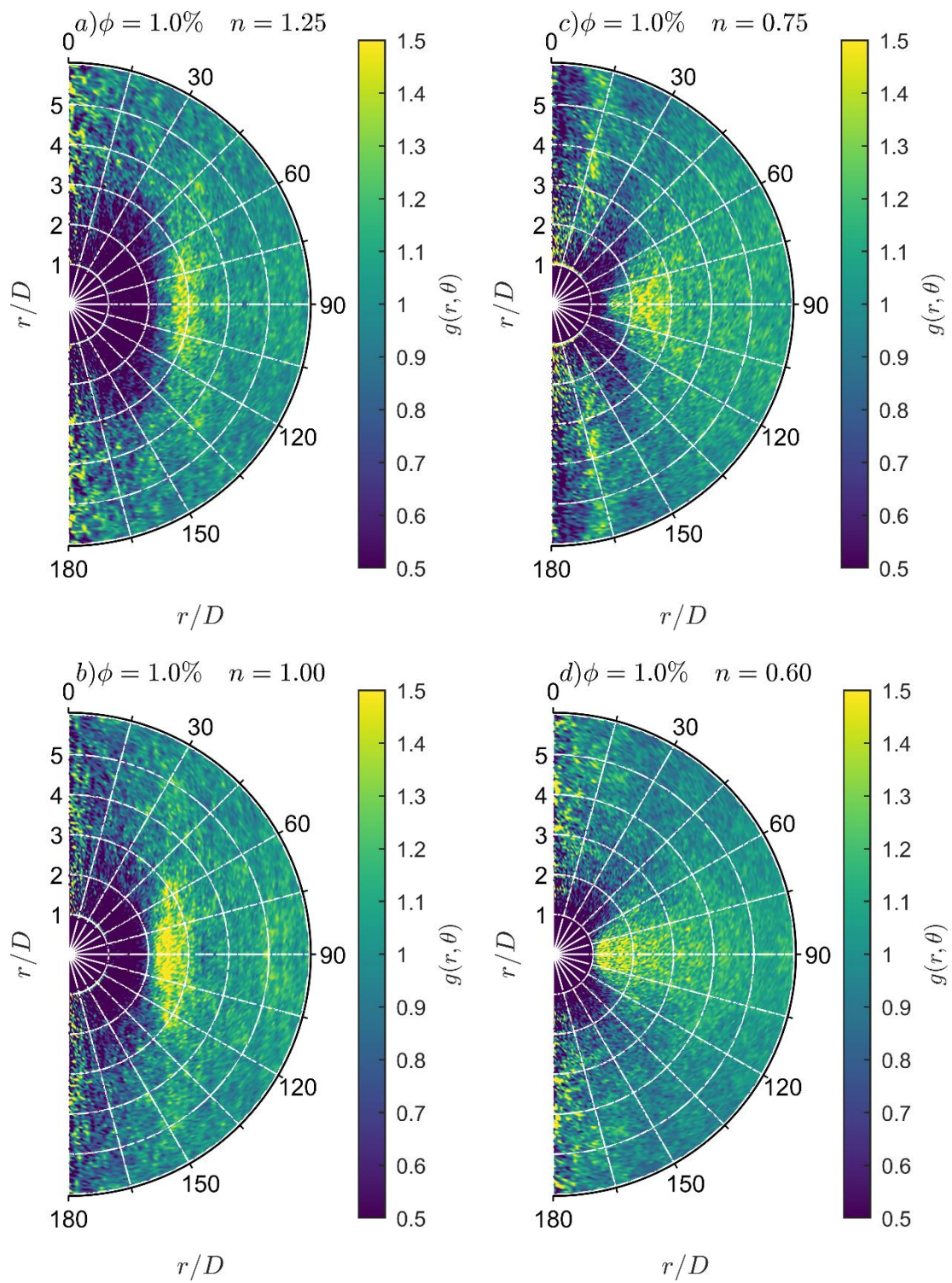


Fig. 12 –Spherical distribution function with $\phi = 1.0\%$ and $Ar = 1000$. (Color in print).

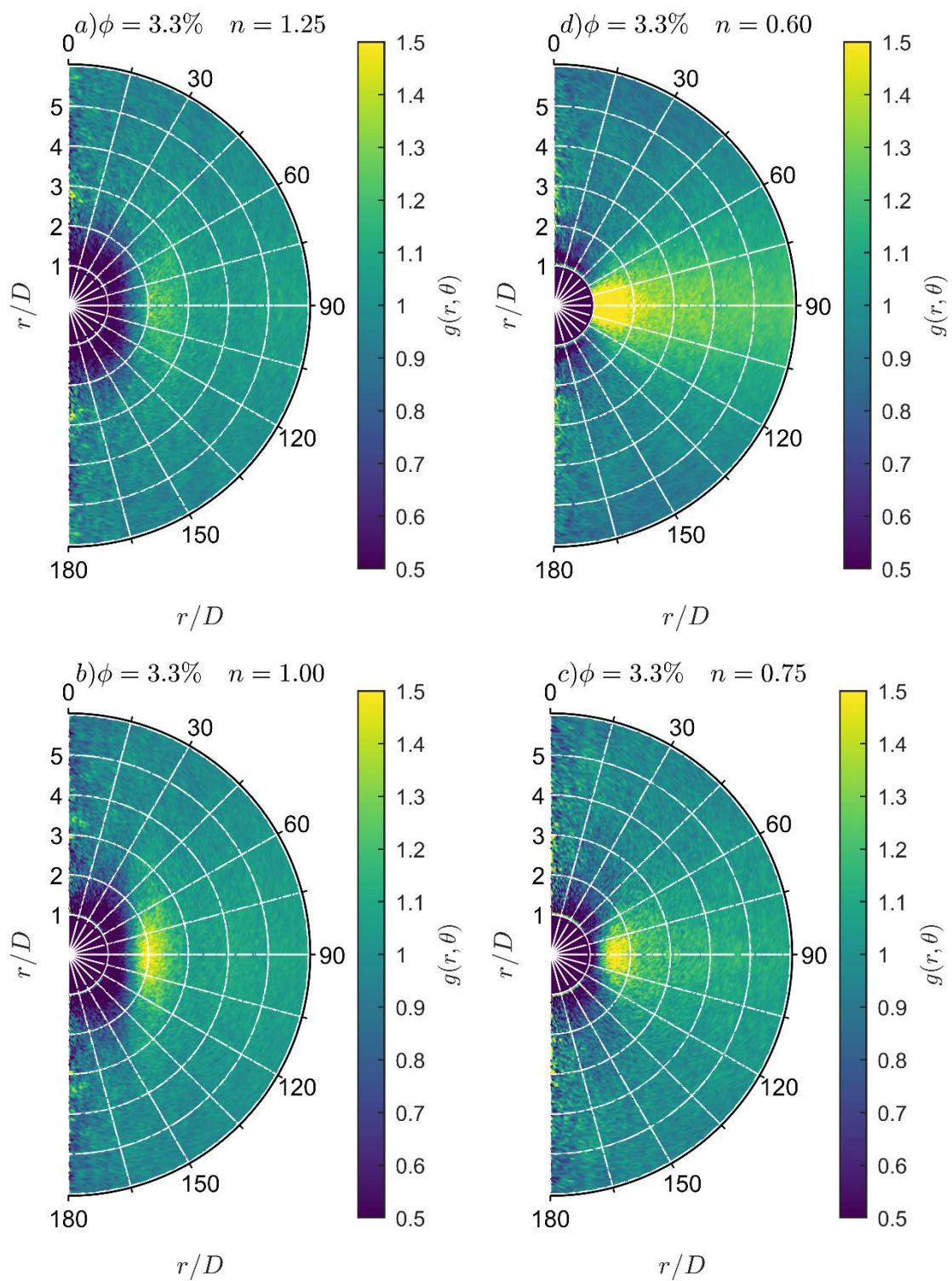
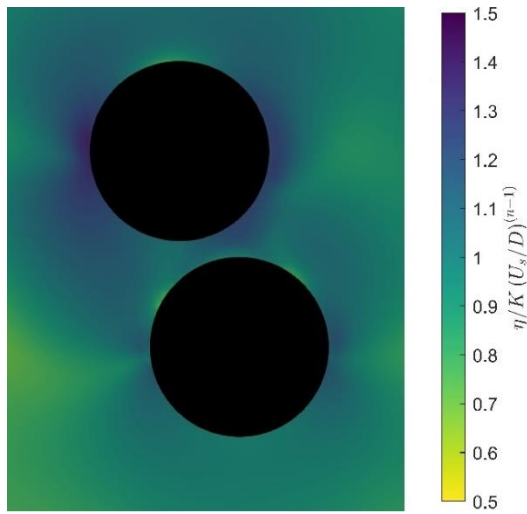


Fig. 13 – Spherical distribution function with $\phi = 3.3\%$ and $Ar = 1000$. (Color in print).

a) $n = 1.25$



b) $n = 0.6$

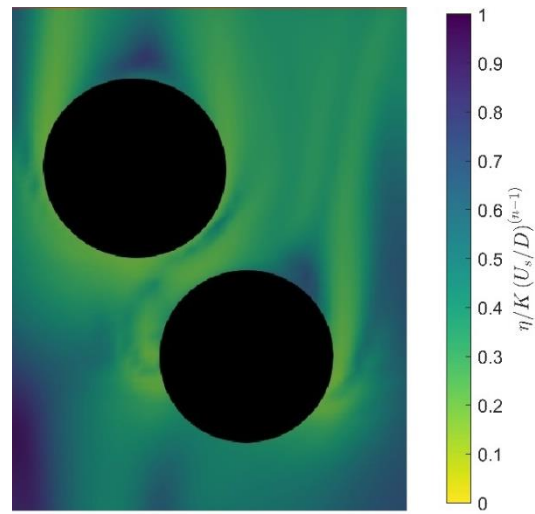


Fig. 14 – Instantaneous viscosity field just before the collision for $n = 1.25$ and $n = 0.6$. (Color in print).

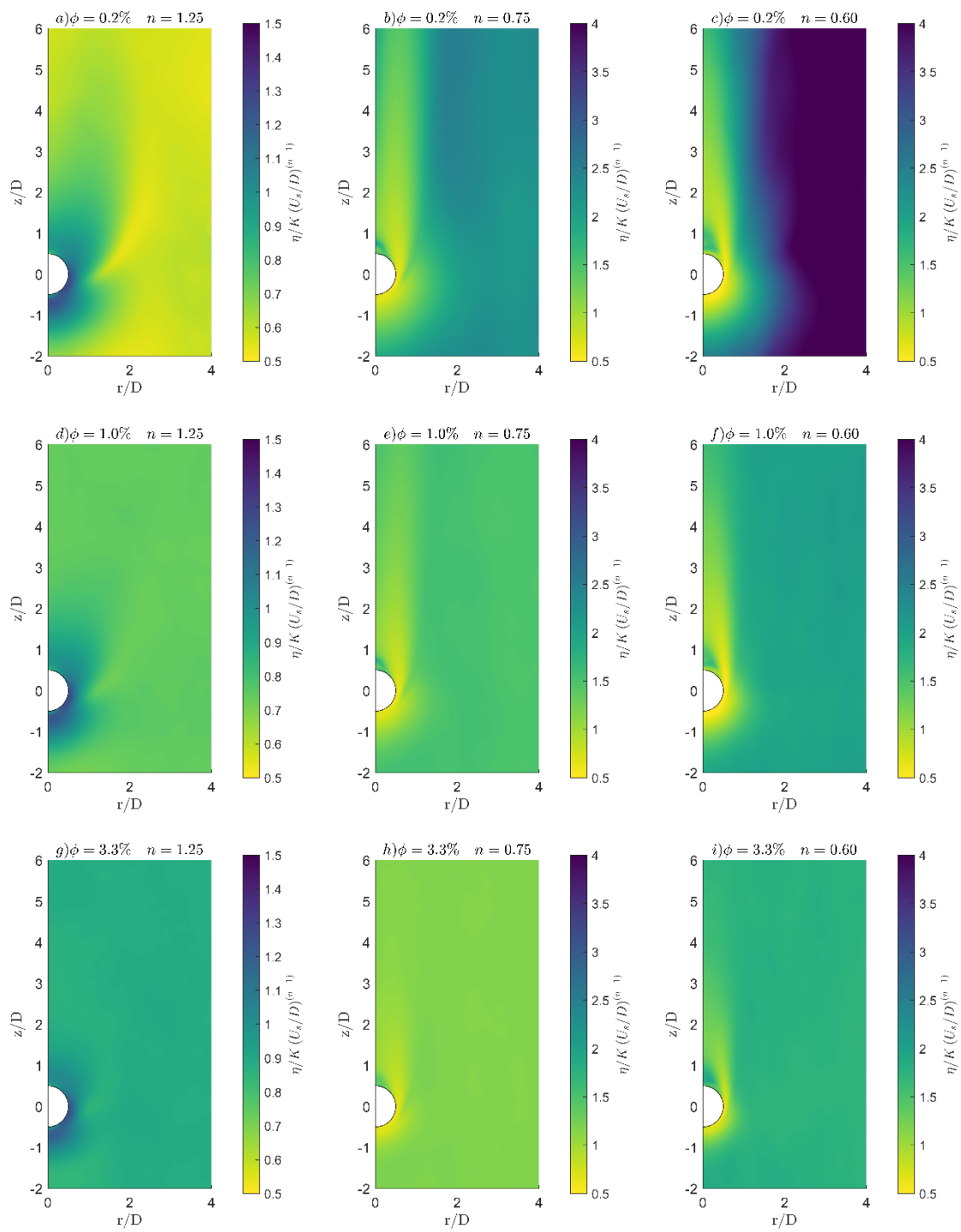


Fig. 15 - Mean viscosity field around settling particles normalized based on the characteristic viscosity $K(U_s/D)^{(n-1)}$. (Color in print).

Table 1 - Particle settling in a power-law fluid. Drag coefficient results and relative error for a spherical particle settling with $\rho_r = 2.25$ and $Ar = 1000$. The Re values are the terminal Reynolds number.

Source	n = 1,25 (Re = 6.91)		n = 1,00 (Re = 18.8)		n = 0,75 (Re = 65.0)		n = 0,60 (Re = 176)	
	C_D	Error	C_D	Error	C_D	Error	C_D	Error
Present Results	5,77	-	2,84	-	1,26	-	0,62	-
Darby [42] apud [9]	4,51	28,0%	2,69	5,5%	1,18	6,2%	0,57	7,5%
Shah et al [43]	2,07	179%	2,73	3,9%	1,21	4,0%	0,43	42,5%
Dhole et al. [44]	5,63	2,5%	2,76	2,8%	1,17	7,4%	0,57	8,3%

Table 2 – Moments and RMS of velocity distribution functions. The mean, standard deviation ($\sigma_{V_{p,z}}$), the skewness ($S_{V_{p,z}}$), and kurtosis ($K_{V_{p,z}}$) are based on the normalized data $(U_{p,z} - U_s)/U_s$.

	N	$\phi = 0.2\%$				$\phi = 1\%$				$\phi = 3.3\%$			
		1.25	1.00	0.75	0.60	1.25	1.00	0.75	0.60	1.25	1.00	0.75	0.60
Settling	$\langle U_{p,z} - U_s \rangle / U_s$	-0.05	-0.07	-0.05	-0.02	-0.14	-0.12	-0.10	-0.07	-0.28	-0.24	-0.20	-0.19
	$\sigma_{V_{p,z}}$	0.08	0.07	0.05	0.07	0.14	0.13	0.11	0.11	0.18	0.15	0.13	0.12
	$S_{V_{p,z}}$	+0.17	+1.61	+1.42	-1.04	+0.58	+0.71	+0.59	-0.53	+0.20	+0.29	+0.28	-0.38
	$K_{V_{p,z}}$	3.40	8.24	10.27	6.09	3.87	4.26	3.91	4.29	3.04	3.13	3.17	3.26
Lateral	$\langle U_{p,xy} \rangle \cdot 10^3$	0.10	-0.65	0.00	-0.22	-0.5	0.10	-0.35	1.01	1.41	0.06	0.04	2.61
	$\sigma_{V_{p,z}} \cdot 10^3$	16.1	14.8	15.3	48.9	42.7	35.2	38.0	68.4	81.9	64.8	63.6	82.1
	$S_{V_{p,z}}$	+0.18	-0.83	+3.39	-0.38	+0.07	-0.01	+0.15	+0.02	-0.01	+0.01	+0.07	-0.02
	$K_{V_{p,z}}$	19.6	70.9	108	4.04	6.13	12.2	16.3	3.37	3.48	4.47	5.35	3.47